



HAL
open science

Disk-resolved photometric modeling and properties of asteroid (101955) Bennu

D. R. Golish, D. N. Dellagiustina, J. -Y. Li, B. E. Clark, X. -D. Zou, P. H. Smith, J. L. Rizos, P. H. Hasselmann, C. A. Bennett, S. Fornasier, et al.

► **To cite this version:**

D. R. Golish, D. N. Dellagiustina, J. -Y. Li, B. E. Clark, X. -D. Zou, et al.. Disk-resolved photometric modeling and properties of asteroid (101955) Bennu. *Icarus*, 2021, 357, 10.1016/j.icarus.2020.113724 . insu-03713793

HAL Id: insu-03713793

<https://insu.hal.science/insu-03713793>

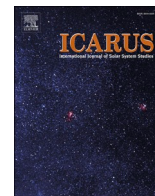
Submitted on 5 Jul 2022

HAL is a multi-disciplinary open access archive for the deposit and dissemination of scientific research documents, whether they are published or not. The documents may come from teaching and research institutions in France or abroad, or from public or private research centers.

L'archive ouverte pluridisciplinaire **HAL**, est destinée au dépôt et à la diffusion de documents scientifiques de niveau recherche, publiés ou non, émanant des établissements d'enseignement et de recherche français ou étrangers, des laboratoires publics ou privés.



Distributed under a Creative Commons Attribution - NonCommercial - NoDerivatives 4.0 International License



Disk-resolved photometric modeling and properties of asteroid (101955) Benu

D.R. Golish^{a,*}, D.N. DellaGiustina^a, J.-Y. Li^b, B.E. Clark^c, X.-D. Zou^b, P.H. Smith^a, J.L. Rizos^d, P.H. Hasselmann^e, C.A. Bennett^a, S. Fornasier^{e,f}, R.-L. Ballouz^a, C. Drouet d'Aubigny^a, B. Rizk^a, M.G. Daly^g, O.S. Barnouin^h, L. Philpottⁱ, M.M. Al Asadⁱ, J.A. Seabrook^g, C. L. Johnsonⁱ, D.S. Lauretta^a

^a Lunar and Planetary Laboratory, University of Arizona, Tucson, AZ, USA

^b Planetary Science Institute, Tucson, AZ, USA

^c Department of Physics and Astronomy, Ithaca College, Ithaca, NY, USA

^d Instituto de Astrofísica de Canarias, La Laguna, Tenerife, Spain

^e LESIA, Observatoire de Paris, Université PSL, CNRS, Université de Paris, Sorbonne Université, 5 place Jules Janssen, 92195 Meudon, France

^f Institut Universitaire de France (IUF), 1 rue Descartes, 75231 Paris CEDEX 05, France

^g The Centre for Research in Earth and Space Science, York University, Toronto, Ontario, Canada

^h The Johns Hopkins University Applied Physics Laboratory, Laurel, MD, USA

ⁱ Department of Earth, Ocean and Atmospheric Sciences, University of British Columbia, Vancouver, British Columbia, Canada

ARTICLE INFO

Keywords:

Photometry
Spectrophotometry
Asteroids
Image processing

ABSTRACT

OSIRIS-REX (Origins, Spectral Interpretation, Resource Identification, and Security–Regolith Explorer) is a NASA mission to return a sample of asteroid (101955) Benu. Photometric modeling of Benu's surface is a key element of both sample site characterization and our broader scientific understanding of the asteroid. Benu's heterogeneous surface presents substantial variation in reflectance and produces a scattered dataset that poses a challenge to photometric modeling. We show that the resolution of the shape model with which we calculate photometric angles strongly affects the accuracy of the analysis, as well as the efficacy of subsequent photometric corrections. We use global imaging data to fit empirical photometric models of the surface. These models represent the average behavior of Benu's surface and can be used beyond this work to photometrically correct panchromatic and color basemaps of Benu and perform albedo analyses of individual features on Benu's surface. Benu's global photometry reveals a moderate opposition effect and detectable phase reddening, both of which suggest a macroscopically rough surface, which is confirmed by centimeter-scale images of the asteroid.

1. Introduction

The primary objective of the Origins, Spectral Interpretation, Resource Identification, and Security–Regolith Explorer (OSIRIS-REX) mission is to return a sample of near-Earth asteroid (101955) Benu (Lauretta et al., 2017). Benu is a low-albedo B-type asteroid with a near-Earth orbit (Hergenrother et al., 2013). Ground observations identified Benu as a primitive body, potentially linked to hydrated carbonaceous chondrites (Clark et al., 2011). The OSIRIS-REX spacecraft was launched in September 2016; surface-resolved imaging began in October 2018 with the OSIRIS-REX Camera Suite (OCAMS; Rizk et al., 2018). Approach observations confirmed Benu's compositional and

spectral characteristics but, contrary to radar observations, revealed a heterogeneous and rugged surface (Lauretta et al., 2019). Before the arrival of the OSIRIS-REX spacecraft at Benu, our understanding of Benu's photometric behavior was limited to disk-integrated, ground-based observations. These showed Benu to have a phase curve slope consistent with other low-albedo asteroids (Hergenrother et al., 2013), but indicated that disk-resolved data would be required to model the surface accurately (Takir et al., 2015). Upon encounter with the asteroid, the high degree of macroscopic roughness validates this prediction and informs our analysis.

Several data products produced by the OSIRIS-REX team, such as panchromatic and color basemaps, rely on the photometric behavior of

* Corresponding author at: 1415 N. 6th Ave., Tucson, AZ 85705, USA.

E-mail address: dgolish@orex.lpl.arizona.edu (D.R. Golish).

<https://doi.org/10.1016/j.icarus.2020.113724>

Received 17 October 2019; Received in revised form 12 February 2020; Accepted 27 February 2020

Available online 5 March 2020

0019-1035/© 2021 The Authors.

Published by Elsevier Inc.

This is an open access article under the CC BY-NC-ND license

(<http://creativecommons.org/licenses/by-nc-nd/4.0/>).

Bennu's surface. The OSIRIS-REx team used these products to help identify potential sampling sites. The photometric models are also used by the navigation team to predict the reflectance of features during sampling for the natural feature tracking (NFT) process, which guides the spacecraft's descent to the surface (Berry et al., 2013; Lauretta et al., 2017). Most importantly, understanding the photometric properties of Bennu, both globally and at the sample site, allows us to put the returned sample into scientific context.

Photometric properties of a surface drive its interaction with light through the incidence (the direction from which the surface is being illuminated), emission (the direction from which the surface is being observed), and phase (the difference between the illumination and observation vectors) angles. These properties depend on surface composition, texture, and morphology (Hapke, 2012; Li et al., 2015; Longobardo et al., 2016), as well as the wavelength of the incident light. We have measured Bennu's surface reflectance under a range of illumination conditions, against which we fit empirical photometric functions. Here we review the challenges that Bennu's surface poses to modeling those observations, the photometric models developed from the imaging data, and the physical interpretation of the model parameters.

2. Photometric observations

We acquire all photometric data with MapCam, the medium-angle color OCAMS imager (Rizk et al., 2018). MapCam has four narrow-band (60–90 nm wide) color filters that mimic the Eight Color Asteroid Survey (ECAS; Zellner et al., 1985) filters. We refer to the filters by their ECAS designation: b' , v , w , and x , with effective wavelengths of approximately 473, 550, 698, and 847 nm, respectively (Golish et al., 2020). The b' filter is slightly redder than its ECAS counterpart, hence its prime designation. MapCam also acquired panchromatic data with its broader filter (~300 nm wide centered at 646 nm).

MapCam photometric observations cover phase angles from 0.7 to 130°. While the lowest phase angle data do not have global coverage, they can be included in this analysis, which treats Bennu as a uniform surface. However, we exclude the highest phase angle data from the analysis due to increased noise. Here we describe the observation campaigns in detail (Table 1).

The OSIRIS-REx spacecraft has carried out several observation campaigns throughout operations. The Approach and Preliminary Survey phases were designed to acquire astronomical and shape modeling data (DellaGiustina et al., 2018; Lauretta et al., 2017), but provided some photometric data. The Detailed Survey phase, however, was dedicated to a global survey of Bennu. Most data used in this investigation were acquired during the Equatorial Stations campaign of the Detailed Survey phase (Lauretta et al., 2017). In this campaign, MapCam imaged Bennu from seven equatorial stations, each at a different local solar hour on the asteroid, measuring the surface at phase angles (α) of 7.5, 30, 45, 90, and 130° (Fig. 1). However, we do not use the 130° phase angle data in this analysis, due to decreased signal-to-noise (Section 4.3). The spacecraft traveled on north-south trajectories in a series of

four-day hyperbolic flybys. For each flyby, MapCam acquired images over a full rotation of Bennu (~4.3 h) while the spacecraft was approximately over Bennu's equator. The spacecraft was ~5 km from the asteroid throughout the observation window. At this distance, a nadir MapCam pixel (Rizk et al., 2018) subtends approximately 33 cm on Bennu. At each station, the spacecraft slewed north-south every 2.7–3° of Bennu rotation, imaging with MapCam's five filters. The camera switched filters between each slew, such that every fifth slew (or every 13–15° of Bennu rotation) imaged with the same filter.

Fig. 1 shows representative images from each station. We model Bennu's photometric response using only MapCam data. Much of the global mapping of Bennu's surface is done with PolyCam, the OCAMS narrow-angle, high-resolution camera, and sample acquisition will be documented with SamCam, the OCAMS moderate field of view, sampling camera (Rizk et al., 2018). However, the MapCam, PolyCam, and SamCam panchromatic bandpasses are similar to within 3% and their detectors are identical (Rizk et al., 2018). Therefore, Bennu appears effectively identical to the three cameras and the photometrical modeling presented here is applicable to all three.

The Bennu local solar times observed during the Equatorial Stations provide a range of rotationally resolved phase angle data, but lack coverage below 7.5° and between 45° and 90°. Therefore, we include images from earlier observation phases—Approach and Preliminary Survey—that observed Bennu at the missing phase angles.

In the Approach mission phase, MapCam imaged Bennu at phase angles between 0.7° and 20° with all five filters. Our investigation only incorporates Approach data where Bennu subtended ≥ 20 pixels to avoid aliasing of point sources (Golish et al., 2020). These observations covered ranges to surface from 320 to 150 m (pixel scales from 22 to 11 m/pixel). Low-phase observations are of particular importance, as OCAMS will not acquire any other images of Bennu with phase angles under 7.5°. As such, they represent our only measurement of Bennu's opposition surge (Section 6.2). During the Preliminary Survey phase immediately following Approach, MapCam acquired images using all five filters, with phase angles ranging from 38° to 90°, as the spacecraft transited along Bennu's equator. Distance to the surface ranged from 9 to 18 km (pixel scale from 60 to 125 cm/pixel). Unlike Equatorial Stations, the data in Approach and Preliminary Survey do not image a complete Bennu rotation. Images from these observation campaigns, at a variety of phase angles, are shown in Fig. 2.

3. Photometric models

Our investigation considered a suite of empirical photometric models (Table 2). We targeted models that are well-suited to describe the behavior of low-albedo surfaces (Li et al., 2015; Takir et al., 2015; Zou et al., 2019). Although Hapke analysis (Hapke, 1986) is a very common method to study photometry of small bodies (Li et al., 2013, 2019; Masoumzadeh et al., 2015; Spjuth et al., 2012), we elect not to include it here for two reasons. Firstly, the pace of mission operations demanded rapid photometric analysis and empirical models are more straightforward to implement quickly. More importantly, the challenge posed by

Table 1

Summary of MapCam photometric observation campaigns. 3:20 am and 8:40 pm data were acquired, but not used in this analysis due to increased noise.

Observation campaign	Phase angle range (°)	Pixel resolution (m/pixel)	Number of images per filter	Global coverage
Approach	0.7–20	11–22	93	No
Preliminary survey	38–90	0.6–1.25	39	No
Equatorial stations – 12:30 pm	7–11	0.32–0.34	70	Yes
Equatorial stations – 10 am	28–32	0.32–0.34	70	Yes
Equatorial stations – 3 pm	43–47	0.32–0.34	70	Yes
Equatorial stations – 6 am	89–93	0.32–0.34	140	Yes
Equatorial stations – 6 pm	89–93	0.32–0.34	140	Yes
Equatorial stations – 3:20 am	130–134	0.32–0.34	95	Yes
Equatorial stations – 8:40 pm	130–134	0.32–0.34	125	Yes

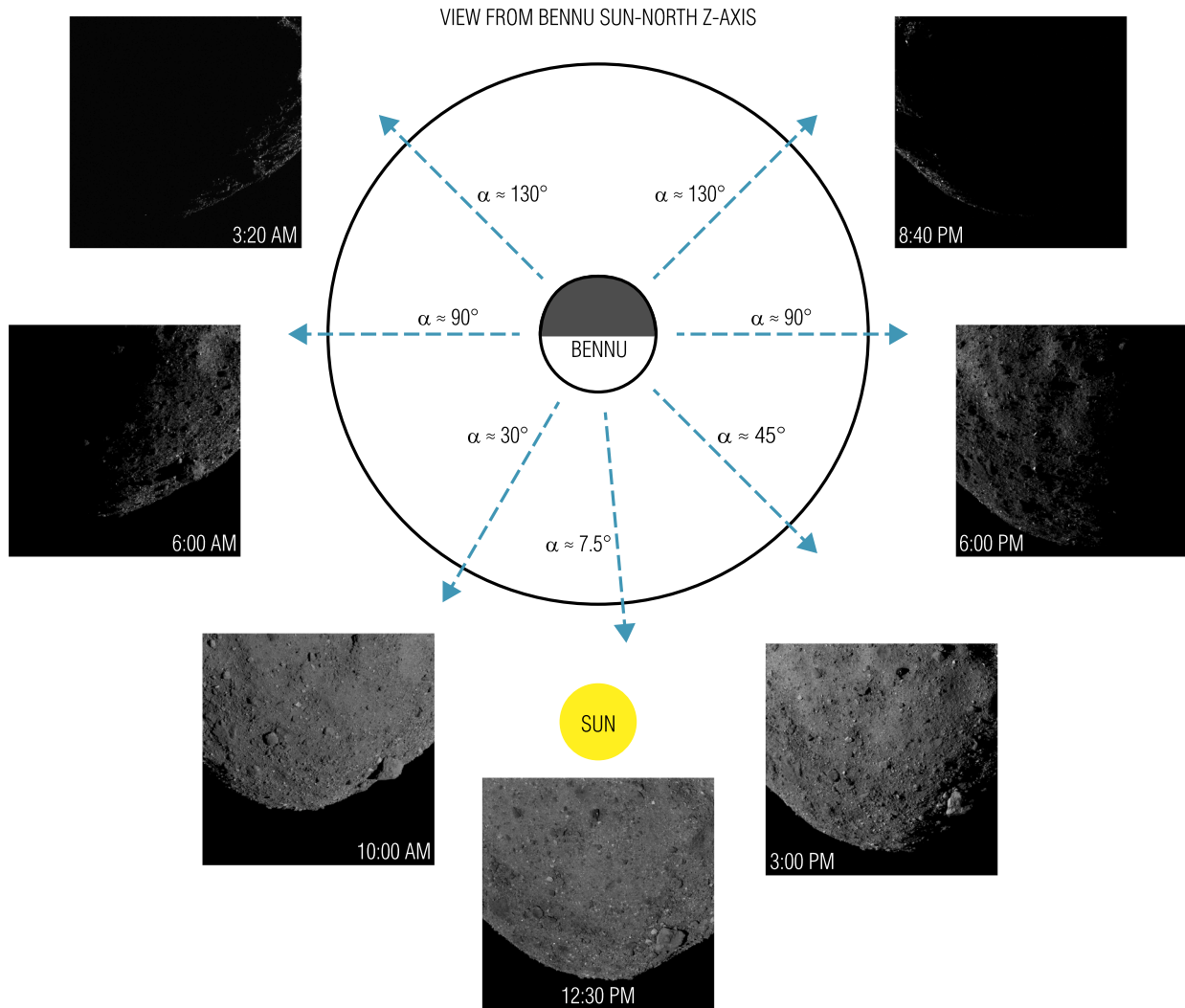


Fig. 1. A schematic of the OSIRIS-REx Equatorial Stations observation campaign. The spacecraft performs hyperbolic flybys at seven local solar times, each for a full Benu rotation, ensuring near-global coverage of Benu's surface. The phase angle (denoted as α) and a representative MapCam image (taken with the v filter) are shown for each station. Images were acquired in north-south slews every $\sim 3^\circ$ of Benu rotation.

Benu's roughness (Sections 4.1, 4.5, 5) is heightened for Hapke analysis, which has more solvable parameters. When high-resolution global shape models become available, the Hapke model will be included in our suite of photometric functions.

Here and throughout this document we express the photometric functions in terms of radiance factor (RADF), also referred to as I/F (Li et al., 2015), where I is the scattered radiance ($\text{W m}^{-2} \mu\text{m}^{-1} \text{sr}^{-1}$) and F is the radiance ($\text{W m}^{-2} \mu\text{m}^{-1} \text{sr}^{-1}$) from a Lambertian surface normally illuminated by the Sun. As such, I/F is dimensionless. The I/F of a surface can be described as a product of a phase function ($A(\alpha)$, describing the phase dependence of the surface reflectance) and a disk function ($d(\alpha, i, e)$, describing how reflectance varies over the surface at a constant phase angle).

$$\frac{I}{F} = A(\alpha)d(\alpha, i, e) \quad (1)$$

Correspondingly, the OCAMS calibration pipeline converts all OCAMS images to units of I/F (Golish et al., 2020). The pipeline also corrects the images for known sources of noise (e.g. dark current, charge smear, and pixel non-uniformity).

The terms i , e , and α denote the incidence, emission, and phase angles, respectively; b and l are the photometric latitude and longitude, respectively; A_{XX} is geometric albedo for a given function; all other

parameters are model coefficients. Geometric albedo is the ratio of the brightness of a body at 0° phase to the brightness of a Lambertian disk under the same conditions (Hapke et al., 1993). Photometric latitude and longitude are photometric parameters calculated following Kreslavsky et al. (2000). The scattering plane is defined as the plane containing the source, surface point, and an observer. The photometric latitude b is the angle between the surface normal and that plane. The photometric longitude l is the angle in the scattering plane between the projection of the surface normal and the vector from the surface point to the observer.

$$\tan(l) = \frac{\frac{\cos(i)}{\cos(e)} - \cos(\alpha)}{\sin(\alpha)} \quad (2)$$

$$\cos(b) = \frac{\cos(e)}{\cos(l)} \quad (3)$$

Prior studies have varied the specific formulation of these photometric models, depending on the planetary surface under consideration (Hapke, 2012; Li et al., 2015, 2019; McEwen, 1986; Schröder et al., 2017; Shkuratov et al., 2011; Takir et al., 2015). To characterize the photometric properties of Benu, we have customized these models for our investigation. Table 2 lists the disk and phase functions used for each model. The Lommel-Seeliger model uses a standard Lommel-Seeliger

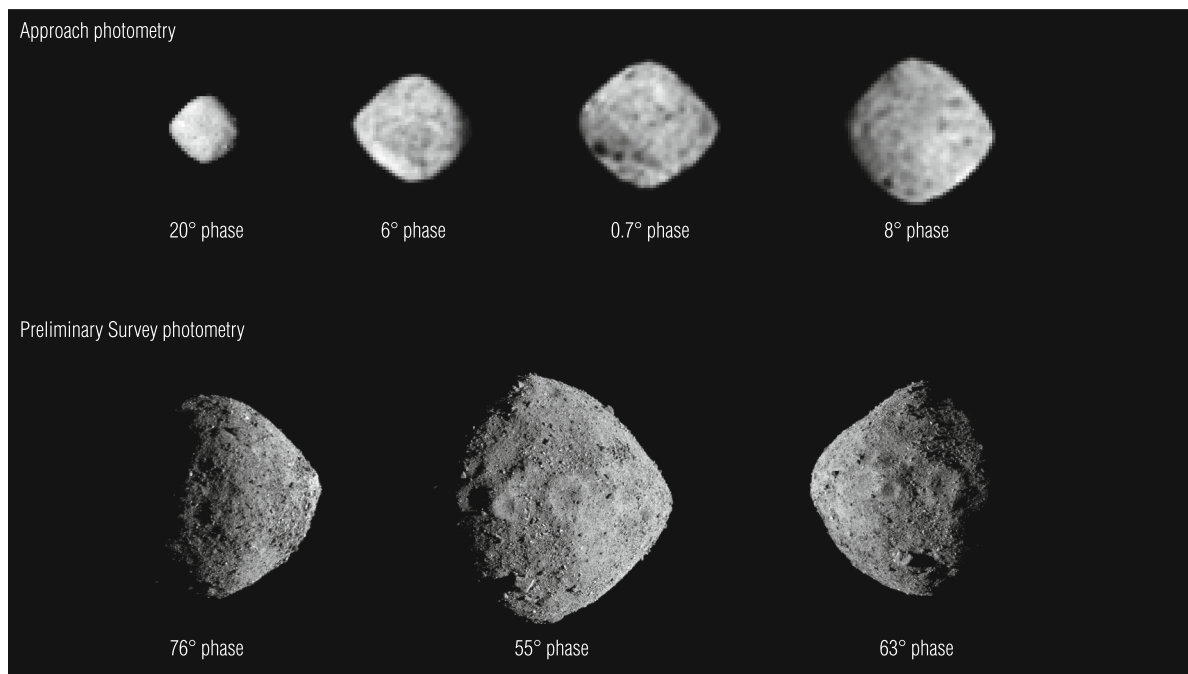


Fig. 2. Representative MapCam (v filter) images from Approach and Preliminary Survey, shown for selected phase angles.

Table 2

The photometric functions used to model OCAMS data, with their disk and phase functions, in terms of RADF.

Photometric function	Disk function – $d(\alpha, i, e)$	Phase function – $A(\alpha)$
Lommel-Seeliger (Hapke, 1981)	$\frac{\cos(i)}{\cos(i) + \cos(e)}$	$A_{LS}\pi e^{\beta\alpha + \gamma\alpha^2 + \delta\alpha^3}$
ROLO (Buratti et al., 2011)	$\frac{\cos(i)}{\cos(i) + \cos(e)}$	$C_0 e^{-C_1\alpha} + A_0 + A_1\alpha + A_2\alpha^2 + A_3\alpha^3 + A_4\alpha^4$
Akimov (Shkuratov et al., 2011)	$\cos\left(\frac{\alpha}{2}\right) \cos\left(\frac{\pi}{\pi - \alpha} \left(1 - \frac{\alpha}{2}\right)\right) \left(\frac{\cos(b)\frac{\alpha}{\pi - \alpha}}{\cos(l)}\right)$	$A_{Ak}\pi e^{\beta\alpha + \gamma\alpha^2 + \delta\alpha^3}$
Linear-Akimov (Li et al., 2019)	$\cos\left(\frac{\alpha}{2}\right) \cos\left(\frac{\pi}{\pi - \alpha} \left(1 - \frac{\alpha}{2}\right)\right) \left(\frac{\cos(b)\frac{\alpha}{\pi - \alpha}}{\cos(l)}\right)$	$A_{LiAk}\pi 10^{-0.4\beta\alpha}$
Lunar-Lambert (McEwen, 1986)	$2L(\alpha) \left(\frac{\cos(i)}{\cos(i) + \cos(e)}\right) + (1 - L(\alpha))\cos(i)$ $L(\alpha) = e^{\alpha\alpha + \zeta\alpha^2 + \eta\alpha^3}$	$A_{LL}\pi e^{\beta\alpha + \gamma\alpha^2 + \delta\alpha^3}$
Minnaert (Takir et al., 2015)	$\cos(i)^{k(\alpha)} \cos(e)^{k(\alpha)-1}$ $k(\alpha) = k_0 + b\alpha$	$A_{Min}\pi 10^{-0.4(\beta\alpha + \gamma\alpha^2 + \delta\alpha^3)}$

disk function (Hapke, 1981) and an exponential phase function (Hapke, 2012). The RObotic Lunar Observatory (ROLO) (Kieffer and Wildey, 1996) photometric function uses a Lommel-Seeliger disk function and a polynomial phase function (Buratti et al., 2011; Hillier et al., 1999). ROLO is the only model used in this work with an explicit opposition surge parameter (Section 6.2). The Akimov model has the advantage of a disk function that minimizes limb brightening as the emission angle approaches 90° (Shkuratov et al., 2011). Here we elect to use the parameter-less form where η is set to 1.0. We have adapted the Akimov model by substituting an exponential phase function, rather than using the sum of exponentials described by Shkuratov et al. (2011). We also include another form (Linear-Akimov) that utilizes the Akimov parameter-less disk function in concert with a linear-magnitude phase function. The Lunar-Lambert model (also called the McEwen model) was originally developed to mimic the lunar disk function (McEwen, 1986). It uses a partition function, $L(\alpha)$, to transition from a Lommel-Seeliger disk function at low phase angles to a Lambertian disk function at high phase angles. The partition function has the same exponential form as the Lommel-Seeliger phase function. Our expression of the Lunar-

Lambert model uses an exponential phase function of the same form as the Lommel-Seeliger model. This treatment allows us to compare the Lunar-Lambert model to the Lommel-Seeliger model and evaluate whether the surface of Bennu follows the Lommel-Seeliger or Lunar-Lambert disk function more closely. The Minnaert model, developed initially for lunar modeling (Minnaert, 1941), has an inverse logarithmic phase function (Takir et al., 2015) like the Linear-Akimov model. Minnaert also has a parameterized disk function, controlled via its limb-darkening parameter, $k(\alpha)$ (Minnaert, 1941). Empirical models with flexible disk functions, such as Lunar-Lambert and Minnaert, can be valuable when attempting to photometrically model a complex surface and have been commonly applied to other planetary bodies (Li et al., 2013; Schröder et al., 2017, 2013).

4. Photometric modeling

The standard inputs to photometric modeling are observation geometry (incidence, emission, and phase angles) and reflectance (Hapke, 2012; Li et al., 2015). Two of the photometric functions used in this

investigation (Minnaert and Lunar-Lambert) have parameterized disk functions. With sufficient data, we can solve for the disk functions simultaneously with the phase functions. However, Benu's rough surface (Lauretta et al., 2019) makes this analysis challenging without global, high-resolution digital terrain models (DTMs) that accurately represent local emission and incidence angles (Section 4.5) at the pixel scale. To improve the fidelity of the models, we solve for the disk functions independently.

4.1. Disk function

We limit the disk function solutions to the Equatorial Stations dataset, which has sufficiently high spatial resolution to track disk function variation. The photometric angles for a given image are calculated using USGS's Integrated Software for Imagers and Spectrometers 3 (ISIS3; Keszthelyi et al., 2013) and SPICE kernels (Acton et al., 2018) provided by the mission. We calculate backplanes for each image (DellaGiustina et al., 2018), including the phase, emission, and incidence angles, with respect to the v28 80-cm-resolution global shape model (Barnouin et al., 2019, 2020). To mitigate the impact of terrain-induced shadowing, and reduce the computation complexity, the images are downsampled from their native 1024×1024 resolution to 128×128 pixels. We further exclude pixels with incidence or emission angles above 82° . The number of remaining pixels per image averages between 10 and 15 thousand for the 7.5° , 30° , and 45° phase images, covering all emission and incidence angles between 0 and 82° . We perform disk function modeling with images in all MapCam filters: 420 images at 7.5° phase and 350 at both 30° and 45° phase. We exclude the high phase angles ($\sim 90^\circ$ and $\sim 130^\circ$) from this fit, as the disk functions are less reliable for those angles. Benu's high degree of macroscopic roughness

causes shadowing (Section 4.5) and results in more scatter in the reflectance data at high phase angles.

We first fit the Lunar-Lambert and Minnaert disk functions to the downsampled data on a per-image basis. Phase angles within a single MapCam image vary by approximately the MapCam field of view of 4° (Rizk et al., 2018). As such, the phase angle dependence of the disk functions in a given image is minimal, and we do not consider it in this analysis. Accordingly, we use the measured reflectance in the images for $d(i, e)$ in Eqs. (4)–(7), forgoing a phase correction. We solve for the disk function parameters, $L(\alpha)$ and $k(\alpha)$, and record them with the median phase angle of the image.

We reformulate the Lunar-Lambert disk function to a linear two-dimensional relationship, where the slope of the fit is the Lunar-Lambert parameter $L(\alpha)$.

$$d(i, e) = 2L(\alpha) \left(\frac{\cos(i)}{\cos(i) + \cos(e)} \right) + (1 - L(\alpha)) \cos(i) \quad (4)$$

$$d(i, e) - \cos(i) = L(\alpha) \left(2 \frac{\cos(i)}{\cos(i) + \cos(e)} - \cos(i) \right) \quad (5)$$

We reformulate the Minnaert disk function to a linear two-dimensional relationship by taking the logarithm of both sides. The slope of the linear fit is then equal to the Minnaert parameter $k(\alpha)$.

$$d(i, e) = \cos(i)^{k(\alpha)} \cos(e)^{k(\alpha)-1} \quad (6)$$

$$\log(d(i, e) \cos(e)) = k(\alpha) \log(\cos(i) \cos(e)) \quad (7)$$

Fig. 3(a–b) plots the photometric data for both formulations, for a single MapCam image acquired at 2019-05-09 20:51:07 UTC at a phase angle of $\sim 8^\circ$, and a linear fit to the distributions. In this example, the

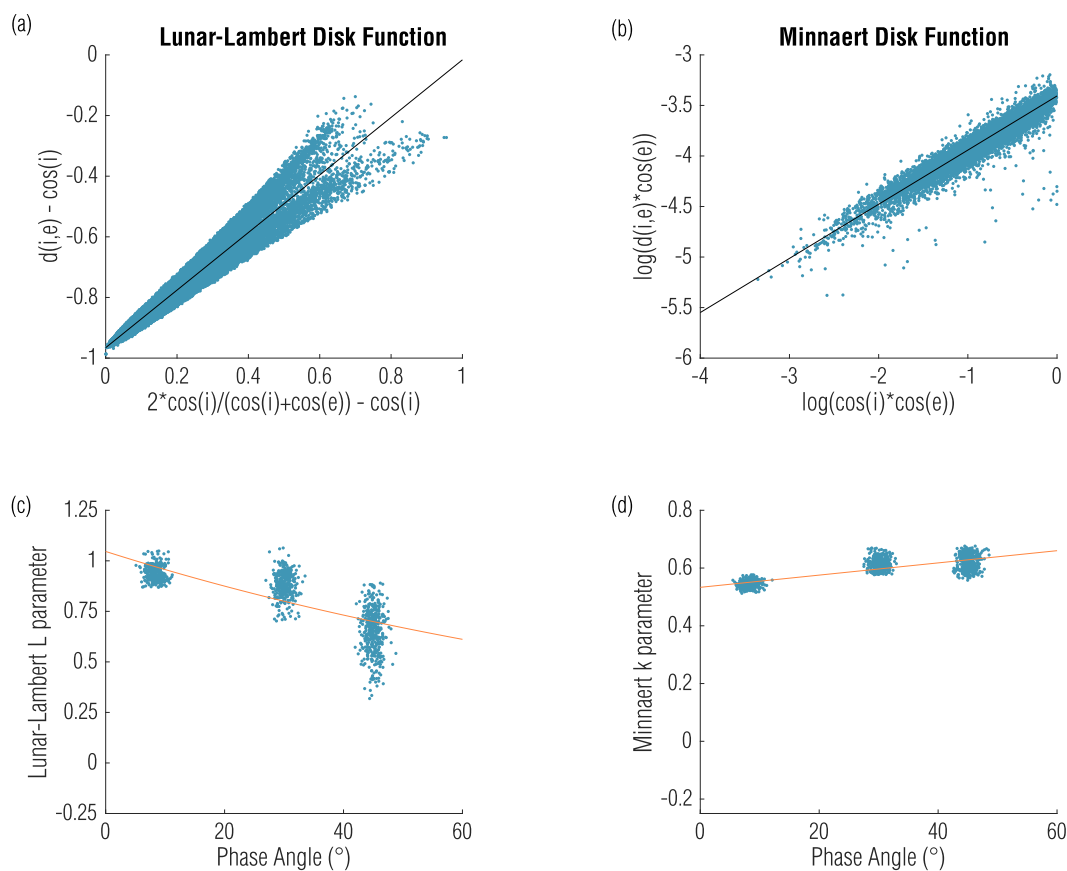


Fig. 3. Fitting a line to the Lunar-Lambert (a) and Minnaert (b) disk functions for a single image provides the L and k parameters, respectively, for each phase angle. We solve for $L(\alpha)$ and $k(\alpha)$ by fitting those parameters for every image as a function of phase angle (c and d). In (c) and (d) the phase angle ranges of the data are artificially broadened to better visualize their density; these data actually vary $<1^\circ$ of phase.

Table 3
Photometric model parameters, and their χ^2 error, for each model and MapCam filter.

Lommel-Seeliger									
Filter	Geometric albedo	A_{LS}	β	γ	δ	χ^2			
pan (646 nm)	0.042	0.0270	-3.395E-02	2.577E-04	-1.579E-06	1.3e-4			
b' (473 nm)	0.042	0.0266	-3.365E-02	2.617E-04	-1.725E-06	1.5e-4			
v (550 nm)	0.042	0.0265	-3.329E-02	2.321E-04	-1.385E-06	1.3e-4			
w (698 nm)	0.040	0.0257	-3.219E-02	2.174E-04	-1.329E-06	1.2e-4			
x (847 nm)	0.039	0.0250	-3.127E-02	1.877E-04	-1.095E-06	1.1e-4			
ROLO									
Filter	Geometric albedo	C_0	C_1	A_0	A_1	A_2	A_3	A_4	χ^2
pan (646 nm)	0.045	0.0101	2.729E-01	7.936E-02	-2.191E-03	3.691E-05	-3.854E-07	1.671E-09	7.6e-5
b' (473 nm)	0.045	0.0099	5.320E-01	8.096E-02	-2.368E-03	4.192E-05	-4.382E-07	1.850E-09	1.0e-4
v (550 nm)	0.044	0.0094	3.615E-01	7.913E-02	-2.184E-03	3.542E-05	-3.519E-07	1.475E-09	7.5e-5
w (698 nm)	0.043	0.0068	5.643E-01	7.962E-02	-2.450E-03	4.805E-05	-5.482E-07	2.450E-09	7.4e-5
x (847 nm)	0.042	0.0060	5.936E-01	7.754E-02	-2.295E-03	4.220E-05	-4.609E-07	2.021E-09	7.7e-5
Minnaert									
Filter	Geometric albedo	A_{Min}	β	γ	δ	k_0	b	χ^2	
pan (646 nm)	0.044	0.0139	3.807E-02	-3.408E-04	1.977E-06	5.300E-01	2.100E-03	1.3e-4	
b' (473 nm)	0.043	0.0137	3.774E-02	-3.454E-04	2.139E-06	5.300E-01	2.100E-03	1.4e-4	
v (550 nm)	0.043	0.0136	3.730E-02	-3.118E-04	1.761E-06	5.300E-01	2.100E-03	1.2e-4	
w (698 nm)	0.042	0.0132	3.610E-02	-2.966E-04	1.709E-06	5.300E-01	2.100E-03	1.1e-4	
x (847 nm)	0.040	0.0129	3.505E-02	-2.634E-04	1.449E-06	5.300E-01	2.100E-03	1.0e-4	
Lunar-Lambert									
Filter	Geometric albedo	A_{LL}	β	γ	δ	ϵ	ζ	η	χ^2
pan (646 nm)	0.043	0.0136	-3.305E-02	2.790E-04	-1.598E-06	-0.009	0	0	1.3e-4
b' (473 nm)	0.042	0.0134	-3.274E-02	2.837E-04	-1.752E-06	-0.009	0	0	1.4e-4
v (550 nm)	0.042	0.0133	-3.233E-02	2.522E-04	-1.398E-06	-0.009	0	0	1.2e-4
w (698 nm)	0.041	0.0129	-3.124E-02	2.385E-04	-1.352E-06	-0.009	0	0	1.1e-4
x (847 nm)	0.040	0.0126	-3.026E-02	2.071E-04	-1.105E-06	-0.009	0	0	1.0e-4
Akimov									
Filter	Geometric albedo	A_{Ak}	β	γ	δ	χ^2			
pan (646 nm)	0.043	0.0136	-3.380E-02	3.025E-04	-1.898E-06	1.2e-4			
b' (473 nm)	0.042	0.0134	-3.348E-02	3.067E-04	-2.048E-06	1.4e-4			
v (550 nm)	0.042	0.0133	-3.310E-02	2.765E-04	-1.706E-06	1.2e-4			
w (698 nm)	0.041	0.0129	-3.202E-02	2.635E-04	-1.665E-06	1.1e-4			
x (847 nm)	0.040	0.0126	-3.099E-02	2.306E-04	-1.407E-06	1.0e-4			
Linear-Akimov									
Filter	Geometric albedo	A_{LiAk}	β	χ^2					
pan (646 nm)	0.040	0.0127	-2.363E-02	3.9e-4					
b' (473 nm)	0.039	0.0126	-2.404E-02	3.4e-4					
v (550 nm)	0.039	0.0125	-2.373E-02	3.5e-4					
w (698 nm)	0.038	0.0122	-2.343E-02	3.0e-4					
x (847 nm)	0.038	0.0120	-2.339E-02	2.5e-4					

disk functions are best fit with $L = 0.950 \pm 0.005$ and $k = 0.536 \pm 0.002$.

We repeat this process for every image, producing a dataset of phase angles and disk function parameters (Fig. 3(c-d)). Both disk functions depend on phase angle; Lunar-Lambert has an exponential dependency and Minnaert has a linear dependency (Table 2). We fit those formulae

to the phase and parameter dataset and calculate the solutions (Table 3).

4.2. Phase function

We solve for the phase functions (Table 2) using a Levenberg-

Marquardt minimization algorithm (a least-squares fitting algorithm used to solve non-linear problems) in the *mpfit* library (Markwardt, 2008) in Interactive Data Language (IDL). For solving the phase functions, we calculate the median reflectance and photometric angles over all pixels in each image (Li et al., 2004; Schröder et al., 2013). We remove pixels with I/F below 0.001 (i.e. unilluminated pixels) and pixels with incidence or emission angles above 82° (where the disk functions are less accurate) before calculating the median. As such, we model Benu as a uniform surface at a disk-resolved scale. This is distinct from disk-integrated photometry where Benu is treated as a whole disk, but we do not yet independently model different surface locations. Long-term analyses will require high-resolution global shape models to photometrically model the surface regionally. We plot the phase function for each model against the disk-corrected reflectance values in Fig. 4. That is, we divide the median reflectance values by the disk function for each model. Consequently, the phase function solves for the equigonal albedo (Kaasalainen, 2001; Shkuratov et al., 2011).

Fig. 4 shows that the solutions track the reflectance data well and are similar to one another. Most of the models underestimate the phase curve at low phase, except for the ROLO model, which includes an explicit term to model the opposition surge (Section 6.2). All models except ROLO and Linear-Akimov slightly overestimate the data in the $45\text{--}85^\circ$ range, where we have only observations from the Preliminary Survey phase, which are lower resolution and do not have global coverage. Nonetheless, the solutions are within the scatter envelope defined by the Equatorial Stations data. The ROLO model appears to fit the reflectance data most consistently and is the only model with an opposition effect term.

We do not plot the phase functions for each wavelength as they only show small differences. However, we observe these subtle differences in each photometric model, suggesting the presence of a spectral dependence in the phase function. We discuss the implications of the most obvious effects—at low and high phase angles—in Sections 6.1 and 6.2.

We compile the solved parameters, as well as the derived geometric albedo, in Table 3 for each filter and photometric model. The albedo terms (A_{XX} for most models, A_0 and C_0 for ROLO) are directly related to the geometric albedo of the surface via the relationships in Table 2. As expected, the geometric albedo decreases with increasing wavelength, matching Benu’s B-type spectrum (Clark et al., 2011; Hamilton et al., 2019; Hergenrother et al., 2013). However, the panchromatic filter’s

albedo is higher than that of all four color filters, which is unphysical; the panchromatic filter spans wavelengths that include the v and w filters and should be similar to those bands. This is an extension of the uncertainties in the radiometric calibration of the panchromatic filter (Golish et al., 2020). The Lunar-Lambert, Akimov, and Lommel-Seeliger phase function parameters are similar, indicating that the different disk functions have a small, but measurable, impact.

We calculate χ^2 values for each model (Table 3), which are all $<1\%$. These error metrics are not absolute measures of quality, but they can be useful for relative comparisons and selecting the optimal model. In this analysis, ROLO consistently has the lowest χ^2 , because it captures the bulk of the phase curve, including the opposition surge. As such, we select it for photometric corrections where albedo calculations (e.g. analyses of individual rocks) are critical.

4.3. High phase data

We do not include 130° phase angle data from the 3:20 AM and 8:40 PM Equatorial Stations in this analysis due to decreased signal-to-noise, as we would expect from lower reflectance (signal) and increased shadows (noise). The χ^2 errors for the photometric solutions increase by as much as 250% (Table 4) when including the high phase data. The Akimov and Linear-Akimov models have the largest increase in error owing to the Akimov disk function poorly correcting the reflectance data at 130° phase. The Lommel-Seeliger and ROLO models have the smallest increase in error, but are at least 10% worse than the models that exclude the 130° phase angle data. This behavior is true for all MapCam filters and is consistent (within 15%) for a given model.

Although the ROLO model only shows a small increase in χ^2 error when using the high phase data, its estimation of the opposition effect (Section 6.2) is degraded. Including the high phase data suppresses the opposition effect slightly. The magnitude of the suppression is 1% absolute albedo and translates directly to an error in albedo estimations of the surface. Moreover, the scatter at high phase varies with wavelength, causing the ROLO opposition effect to vary by an additional 1–2% in absolute albedo. This variation will manifest, when applied as a photometric correction, as changes in Benu’s spectrum that are not realistic.

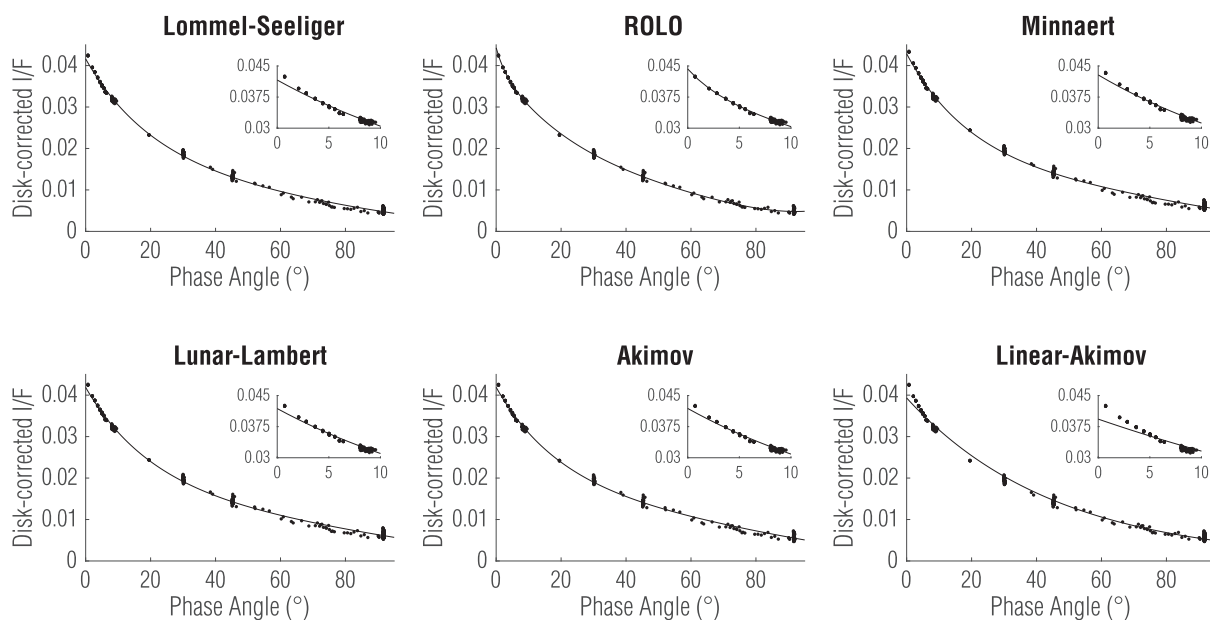


Fig. 4. Phase functions (solid lines) are fit to disk-corrected reflectance data for each photometric model, shown here for MapCam’s v filter. Insets show low phase angles, at which only the ROLO model accurately captures the opposition effect.

Table 4
 χ^2 error for each photometric model solution, per filter, when including 130° phase angle data.

Filter	Lommel-Seeliger	ROLO	Minnaert	Lunar-Lambert	Akimov	Linear-Akimov
pan (646 nm)	1.7e-4	8.9e-5	2.1e-4	1.8e-4	3.0e-4	7.8e-4
b' (473 nm)	2.0e-4	1.2e-4	2.4e-4	2.2e-4	3.4e-4	7.0e-4
v (550 nm)	1.5e-4	8.4e-5	1.8e-4	1.6e-4	2.6e-4	7.2e-4
w (698 nm)	1.6e-4	9.0e-5	1.9e-4	1.6e-4	2.7e-4	6.5e-4
x (847 nm)	1.3e-4	9.2e-5	1.5e-4	1.4e-4	2.3e-4	5.9e-4

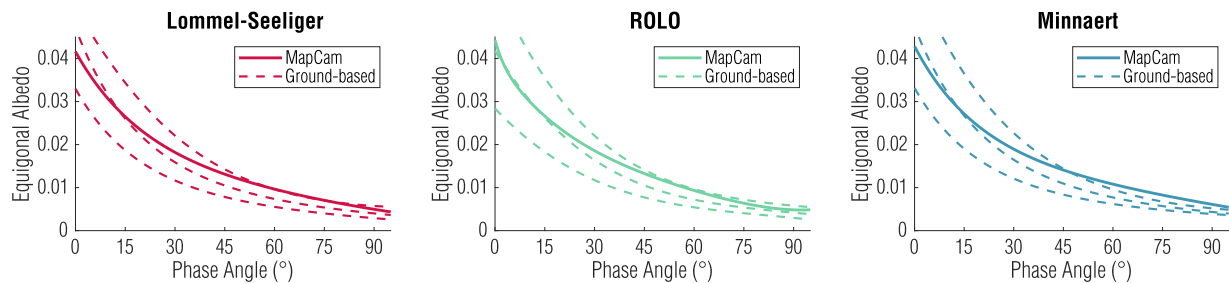


Fig. 5. Comparison of OCAMS (MapCam, solid lines) and ground-based (dashed lines) photometric models shows agreement at low phase angles, where the disk-resolved and disk-integrated methods are most similar. The three ground-based models represent the range of potential models, based on different assumptions for Bennu's albedo (Takir et al., 2015).

4.4. Comparison to ground-based observations

We can compare ground-based, disk-integrated photometric analyses of Bennu (Takir et al., 2015) and our disk-resolved models. The ground-based work performed disk-integrated analyses using Lommel-Seeliger, ROLO, and Minnaert models. In Fig. 5, we plot the models developed in this work (solid lines) with the nominal, minimum, and maximum models from Takir et al. (2015) (dashed lines). The nominal ground-based model includes reduced v magnitude data from asteroid Mathilde to fill in phase angles that were not observed for Bennu. The maximum and minimum models attempt to capture the potential variation in Bennu's brightness. The nominal models are in good agreement with our disk-resolved models at low phase ($<15\%$ difference for $\alpha < 30^\circ$). All three methods deviate from the disk-resolved models at mid- to high-phase angles; the OCAMS models have a shallower phase curve slope than the nominal ground-based models. This deviation is consistent with initial photometric observations of Bennu from the Approach phase (Hergenrother et al., 2019). Nonetheless, the disk-resolved models fall largely within the envelopes defined by the ground-based analysis, which in turn have a shape similar to other dark asteroids such as Ceres and Mathilde (Longobardo et al., 2019, 2016). Moreover, the geometric albedos derived from these models (Table 3) agree with ground-based measurements of 0.046 ± 0.005 (Emery et al., 2014), as well as measurements of CI and CM chondrites (Clark et al., 2011).

4.5. Sources of uncertainty

The uncertainty in the radiometric calibration of the camera (Golish et al., 2020) directly affects photometry, but is limited to the albedo terms (Table 3). Except for ROLO, the models considered in this study have an albedo term that is a multiplicative scalar of the phase function, A_{XX} . For the ROLO model, two parameters control the albedo: the multiplicative scalar in front of the exponential (opposition surge) term and the additive scalar in front of the polynomial phase function, A_0 and C_0 .

Image-to-image radiometric variation is negligibly low in the photometric data for two reasons. The SNR of individual pixels is >100 , imparting $<1\%$ error due to shot noise. More importantly, the photometric pipeline calculates the median of 300,000 to 1 million pixels (depending on the amount of shadowing) for an image; this further reduces stochastic noise by 2–3 orders of magnitude.

Nonetheless, it is evident from Fig. 4 that there is scatter in the reflectance data, even after disk-correction. In part, this represents imperfect disk corrections, due either to an empirical form that does not perfectly describe the surface or to an imperfect solution for the disk function parameters. It is also indicative of a heterogeneous surface with a range of intrinsic albedos (Lauretta et al., 2019). However, the primary contributor is likely the substantial terrain-induced reflectance variation on the surface. The spatial resolution of the Equatorial Stations images is approximately 33 cm/pixel; the size frequency distribution of Bennu's boulders (DellaGiustina et al., 2019) suggests hundreds of boulders larger than 3 m (~ 10 pixels) in a typical MapCam Equatorial Stations image. Each will cast a shadow with similar width (and with a length dependent on the local solar time of the station). As we image further from the equator, incidence angles will increase and shadows will lengthen. Correspondingly, the bright face of rocks will be oriented toward the Sun with low incidence angles, even when we observe the underlying surface at relatively high incidence angles. Fig. 6 illustrates this by plotting normalized histograms of the incidence and emission angles using global medium-resolution (left) and local high-resolution (right) shape models of a PolyCam image taken at 2019-03-28 19:24:10 UTC, with a center latitude/longitude of $(-8^\circ, 110^\circ)$. The relatively narrow medium-resolution histogram captures the global variation in the image. The broader high-resolution histogram also captures the variation due to individual boulders. The global shape model used in this analysis has a ground sample distance (GSD) of ~ 80 cm. As such, the photometric backplanes do not capture the high-frequency variation, which therefore does not contribute to the photometric statistics. Using a local high-resolution model produced by the OSIRIS-REx Laser Altimeter (OLA; Daly et al., 2017) with a ~ 10 -cm GSD captures nearly all of the terrain variation visible at this image resolution (~ 5 cm/pixel) and shifts the median emission angle by $\sim 10^\circ$. Shifts such as this will be present in every image, for both incidence and emission angle, with magnitude and direction that depend on the terrain in the image. The offsets couple directly, and non-linearly, into both solving the disk function (Section 4.1) and removing the disk function when solving for the phase function (Section 4.2).

Moreover, we calculate reflectance values and photometric angles on a per-image basis. This excludes extremely low (<0.001) reflectance pixels and removes deep shadows, but it cannot remove gradual shadows. It also excludes very high ($>82^\circ$) emission and incidence angles, but those angles come directly from the global shape model, which

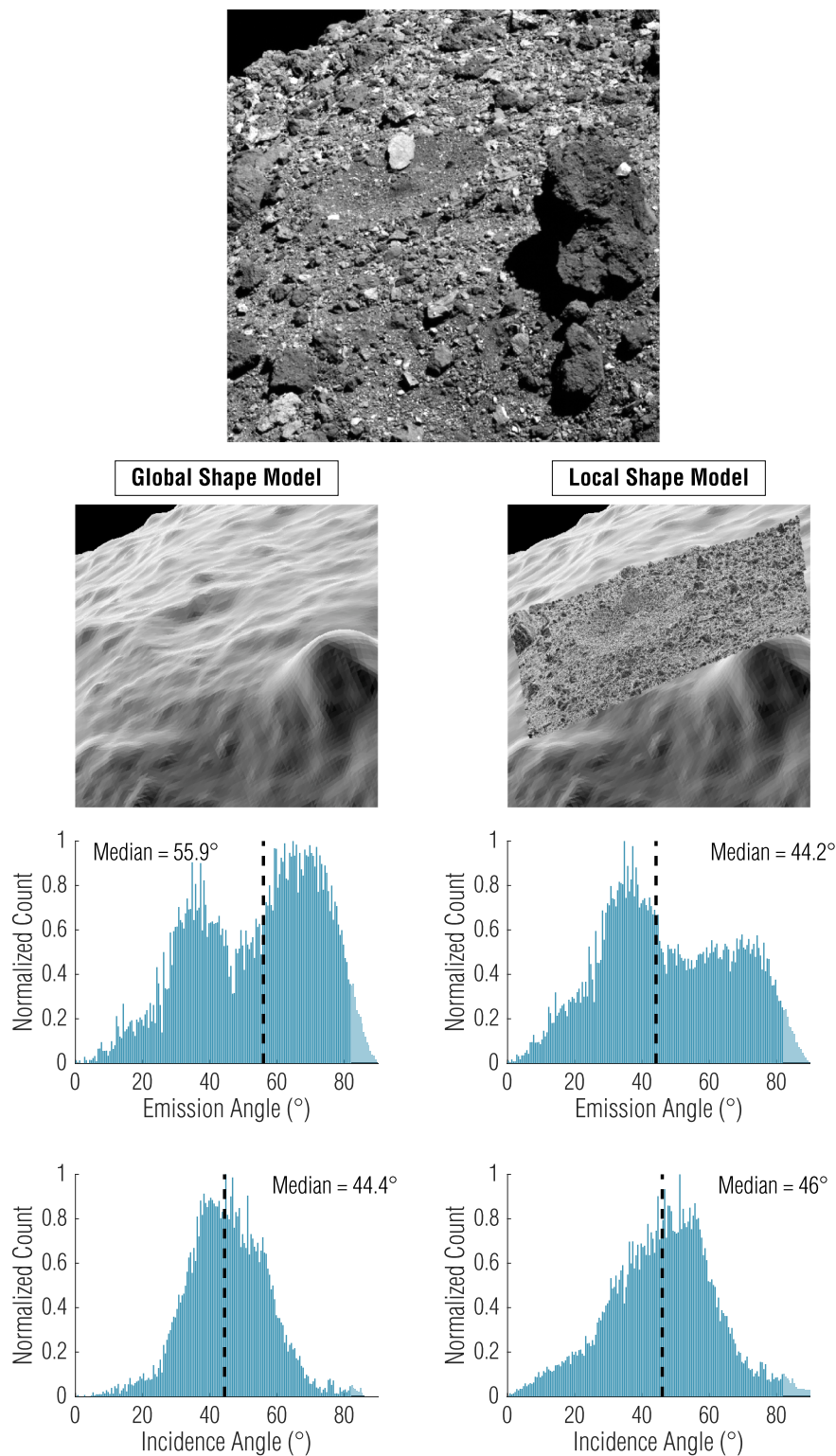


Fig. 6. Normalized histograms of emission and incidence angle using medium-resolution (global) and high-resolution (local) shape models demonstrate median shifts that perturb global photometric modeling. Emission and incidence angles over 82° are not included in the calculation.

does not accurately represent features below its resolution. Even for large features, their topography is limited by the vertical accuracy of the shape model (Barnouin et al., 2019). As such, the photometric angles of large features are underrepresented and small features are missing. However, the reflectance variation due to their photometric orientation is included in the median reflectance of an image. Bright rock faces will boost the median reflectance but are not captured in the median

emission and incidence angles. Combined with imperfect shadow removal, the disk-corrected reflectance data have increasing noise with increasing phase angle.

We have not yet quantified the reflectance scatter due to these effects and its contribution to the photometric model solutions is difficult to assess. Traditional error bars on the parameters in these fits have limited utility because the parameters are interdependent, i.e., there is not

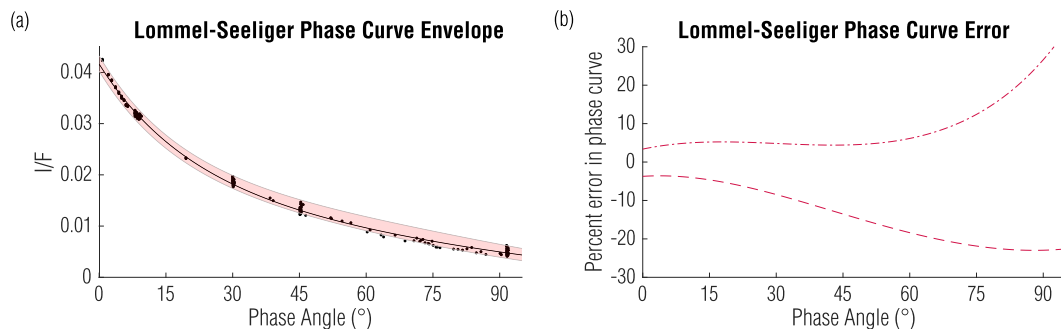


Fig. 7. Independently fitting phase curves to the top and bottom of the reflectance variation from each Equatorial Station produces an envelope of potential phase functions (a). This envelope represents the worst-case photometric modeling error imparted by terrain-induced reflectance variation that is not represented in the global shape model (b).

necessarily a unique solution. This is particularly true for empirical models with polynomial components, which includes all of the models presented here except Linear-Akimov. However, we can use the scatter in the reflectance data itself to predict its effect. Because the six photometric models and five filters are similar, we use the v filter with a Lommel-Seeliger model to perform this analysis. We take the reflectance points from each Equatorial Station and separate them into clusters at either end of the range of variation. We are effectively separating the population into a maximum and minimum reflectance group, against which we re-fit the Lommel-Seeliger model. This allows us to solve for an envelope of phase functions that bound the observed photometric response of Benu.

Fig. 7(a) shows a phase function envelope that represents the potential shift of the phase function due to these errors; Fig. 7(b) plots the error imposed by these worst-case models. At low phase angles ($<30^\circ$), where we are most likely to make reflectance/albedo measurements, the error envelope is below 5%. At mid and high phase angles, the error surpasses 20%. We emphasize that these are worst-case uncertainties defined by the maximum variation in our reflectance data, due to the variety of effects discussed here. Table 5 lists the Lommel-Seeliger parameters for the nominal, minimum, and maximum solutions; these parameters emphasize the fact that traditional error bars on polynomial terms are ineffective, as both the minimum and maximum cases have polynomial terms that deviate in the same direction from the nominal case. Subsequent photometric studies that can utilize global high-resolution shape models will be able to decrease the reflectance scatter and reduce the size of the envelope.

5. Influence of shape model resolution on photometric correction

A useful metric for the efficacy of photometric modeling is the quality of the resulting photometric correction (Denevi et al., 2018). For many of the data products that we create throughout operations, our goal is to make seamless maps; photometric correction is critical for these products (Bennett et al., 2020). Photometric correction is implemented by multiplying the measured signal by the ratio of the model reflectance at a standard geometry (typically 30,0,30 or 0,0,0; Hicks et al., 2011; McEwen, 1991; Yokota et al., 2011) to the model reflectance at the measured geometry.

Table 5
Lommel-Seeliger phase function parameters for the phase curve error envelope.

	A_{LS}	β	γ	δ
Nominal	0.0265	$-3.329e-2$	$2.321e-4$	$-1.385e-6$
Maximum	0.0276	$-3.403e-2$	$3.354e-4$	$-2.136e-6$
Minimum	0.0264	$-3.563e-2$	$3.252e-4$	$-2.409e-6$

$$\left(\frac{I}{F}\right)_{corr} = \left(\frac{I}{F}\right)_{meas} \frac{A(\alpha_{std}) * d(\alpha_{std}, i_{std}, e_{std})}{A(\alpha_{meas}) * d(\alpha_{meas}, i_{meas}, e_{meas})} \quad (8)$$

However, as with modeling, the resolution of the shape model limits the accuracy of the photometric correction. This is especially true on Benu, with macroscopic roughness at the same spatial scale as our image data. When a feature (e.g. a rock face) is oriented differently than the underlying surface, and that feature is not resolved in the shape model, the i_{meas} and e_{meas} terms will be incorrect, leading to an imperfect photometric correction. We demonstrate this qualitatively in Fig. 8, which shows a PolyCam image, photometrically corrected with global 80-cm-resolution and local 10-cm-resolution shape models. Though the registration errors between the image and the local 10-cm-resolution shape model produce some high-frequency highlights, the overall correction is much more accurate (i.e., has a flatter appearance) than with the global 80-cm-resolution model. The small bright rock in the insets appears $\sim 50\%$ brighter than its surroundings when corrected with the 80-cm-resolution global shape model. Correction with the 10-cm-resolution local shape model reveals that the rock has a similar albedo to the background. Moreover, relatively large shape model facets in the global model can introduce low-frequency highlights such as the one seen on the upper-left corner of the large flat rock at the northern edge of the crater. This simple example is representative of photometric correction artifacts across the surface of Benu, which can be universally described as rough at these length scales. Indeed, for any surface, the resolution of a shape model must match the length scale of the terrain variation. Benu's roughness merely exaggerates the effect in OCAMS images. The sensitivity of photometric correction to shape model resolution is particularly important for analysis of individual features (e.g. boulders) on the surface.

6. Implications for photometric properties of Benu

6.1. Phase reddening

Phase reddening is a photometric effect commonly observed on airless bodies (Li et al., 2015) and manifests as spectral reddening at increasing phase angle (Gradie and Veverka, 1986). We explore the extent of phase reddening by calculating ratios of the phase curves for MapCam's filters. We calculate these ratios with respect to the v filter at 7° phase, such that the separation of the b'/v and x/v curves are indicative of the degree of phase reddening. Normalizing at 7° omits the impact of the opposition surge, which is slightly blue in the ROLO model (consistent with the analysis in Section 6.2). We do so for each photometric model and plot the results in Fig. 9. The consistency of the models is encouraging, as each demonstrates $\sim 5\%$ phase reddening at 90° phase.

Wavelength dependence of the phase function is commonly attributed to multiple scattering, as it causes longer optical path lengths and

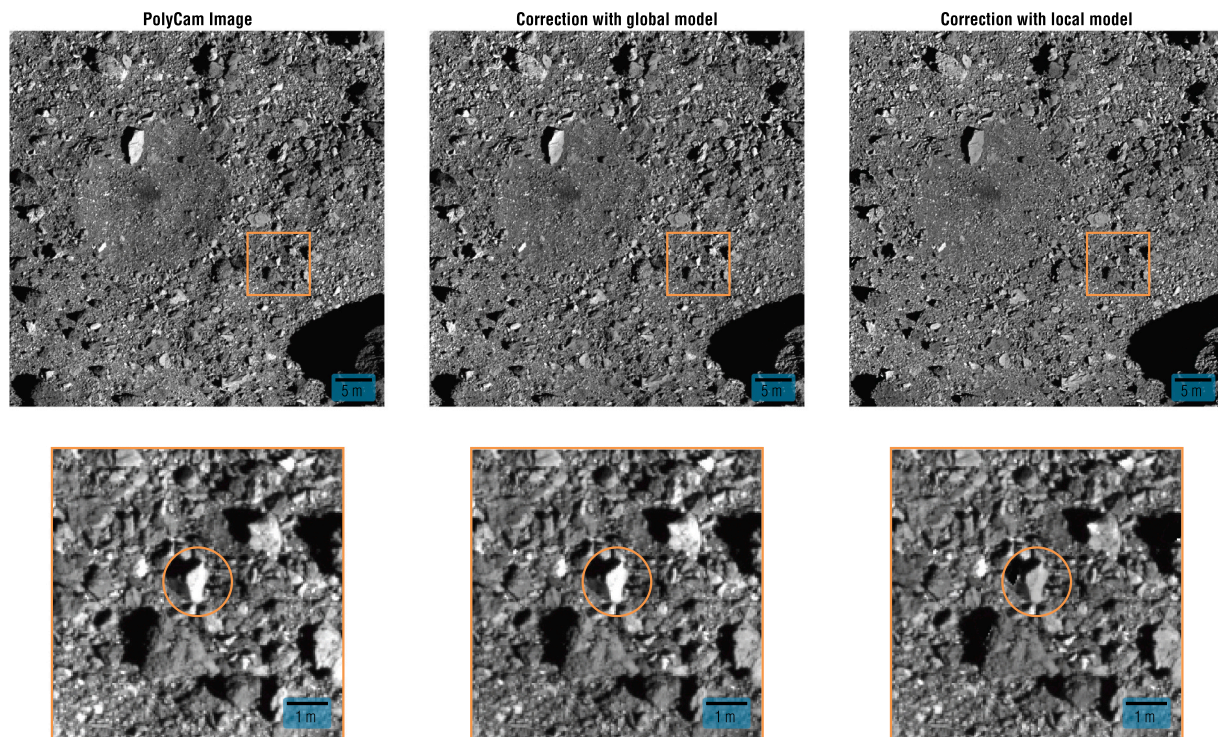


Fig. 8. The resolution of the shape model used to photometrically correct a PolyCam image (acquired 2019-03-29 21:10:16) has a large effect on the accuracy of the result. The encircled rock appears bright in an image that is photometrically corrected with an 80-cm-resolution global shape model. Correction with a 10-cm-resolution local shape model corrects its reflectance to be closer to the surrounding terrain.

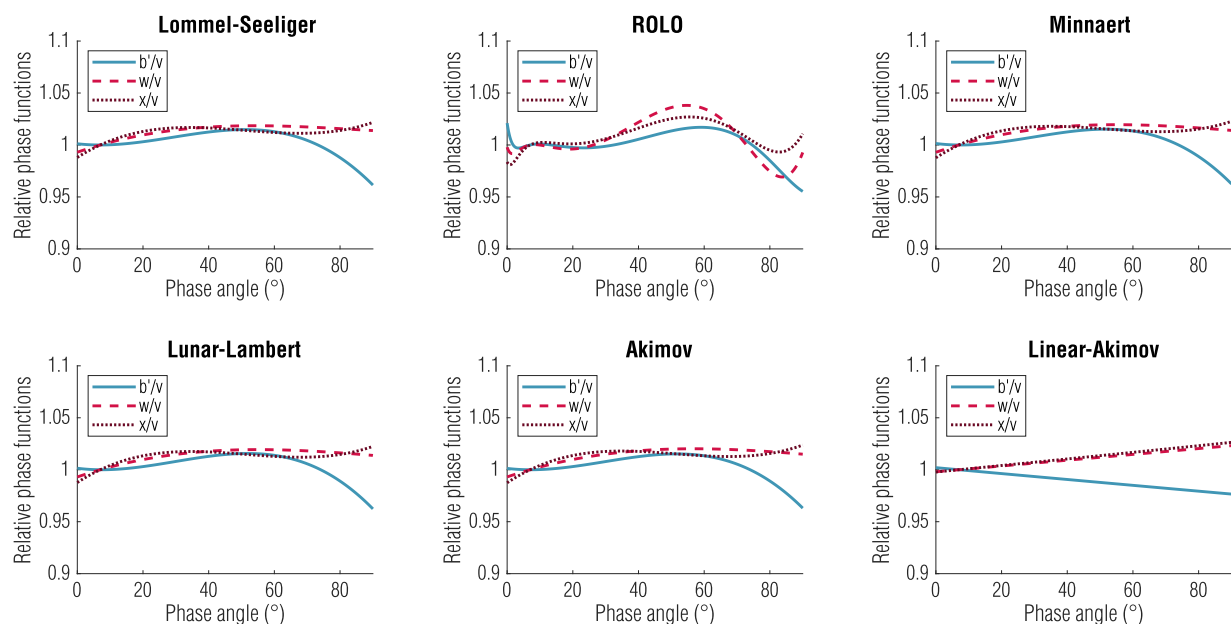


Fig. 9. Normalizing the b' (473 nm), w (698 nm), and x (847 nm) filters to the v (550 nm) filter at 7° phase illustrates $\sim 5\%$ phase reddening at 90° phase.

therefore more absorption in bluer wavelengths (Schröder et al., 2014). In this context, however, Bennu’s low albedo suggests a single-scattering surface (Muinonen et al., 2002) and limited wavelength dependence, yet we observe a small degree of phase reddening (Fig. 9). In DellaGiustina et al. (2019), we proposed that Bennu may be analogous to Ceres, another dark object ($\sim 9\%$ albedo; Li et al., 2016) that exhibits phase reddening. Ceres shows stronger phase reddening ($\sim 15\%$ over OCAMS’s wavelength range) than Bennu. Li et al. (2019) suggested that phase reddening might be due to the presence of micron-scale surface

roughness or particles.

On Ceres, multiple lines of evidence pointed to submicron grains as the most likely mechanism (Li et al., 2019). However, recent Mobile Asteroid Surface Scout (MASCOT) results from the Hayabusa2 mission at asteroid Ryugu (Jaumann et al., 2019) show no evidence of a dust covering on that asteroid, despite its low thermal inertia (Sugita et al., 2019). This finding seems to contradict the conventional expectation that low thermal inertia is due to a small average grain size (Gundlach and Blum, 2013), but MASCOT thermal measurements have eliminated

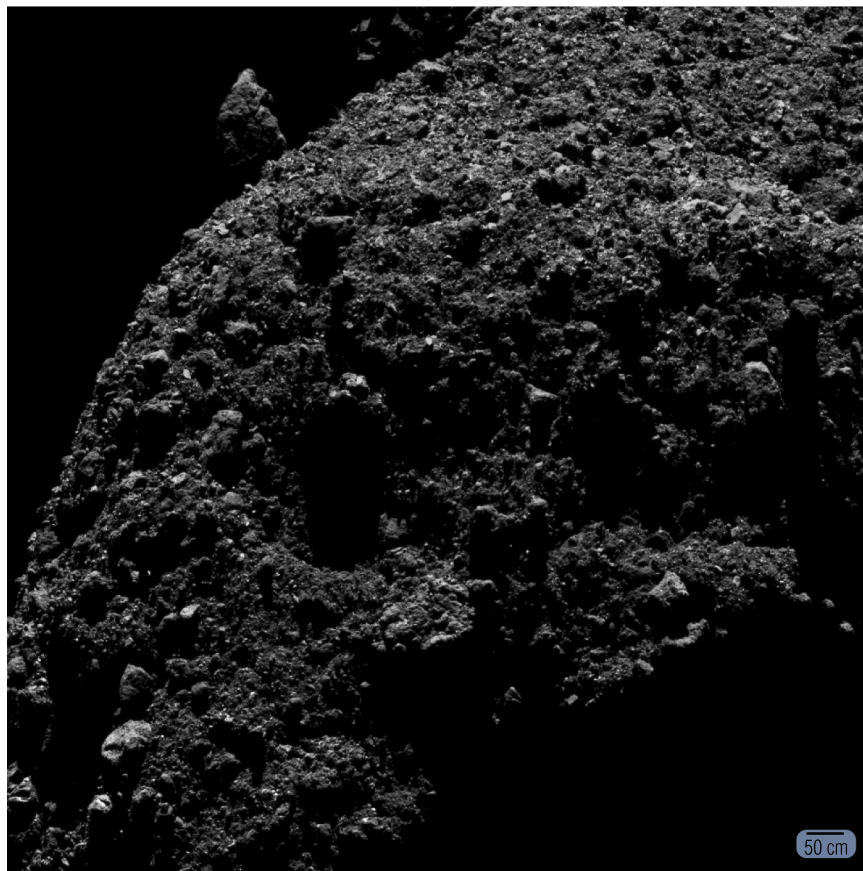


Fig. 10. High-resolution (~1 cm/pixel) imaging of Benu's surface, such as this image acquired at 2019-07-30 13:01:47, shows an extremely rough surface texture that likely increases optical path lengths, causing reddening at high phase angles.

the possibility of an optically thick layer on Ryugu while confirming its low thermal inertia (Grott et al., 2019). As Benu and Ryugu are both near-Earth asteroids with similar degrees of macroscopic roughness, we might expect Benu to exhibit similar behavior. Moreover, as OSIRIS-REx studies Benu in increasing detail, we see continued evidence of porous, rough surface features at the centimeter scale (Fig. 10). Macroscopic roughness has been linked to wavelength-dependent phase response (Pilorget et al., 2016), which promotes the idea that surface structure might contribute to Benu's modest phase reddening. As higher-resolution shape models become available, regional photometric modeling of Benu's surface, and corresponding indicators of surface roughness whether through visual inspection or thermal analyses, will be able to evaluate this link.

6.2. Opposition surge

The opposition surge is a phenomenon on most planetary bodies wherein the reflectance of a surface increases dramatically as phase angle approaches 0° (Irvine, 1966). It is typically modeled as the combination of two effects – the coherent backscatter opposition effect (CBOE) and the shadow hiding opposition effect (SHOE). CBOE occurs when independent electromagnetic waves scatter off a surface and constructively interfere (Hapke, 2012). This coherent backscatter can only occur at very low phase angles, where the waves travel nearly identical optical path lengths and is typically dominated by multiple scattering. SHOE occurs when a particle obstructs an observer's view of the particle's shadow, which can only occur at low phase (Hapke, 2012). This effect is driven by particle size and macroscopic surface roughness.

OSIRIS-REx did not acquire any images or spectra at 0° phase, but MapCam did acquire images from 0.7 to 20° phase during Approach.

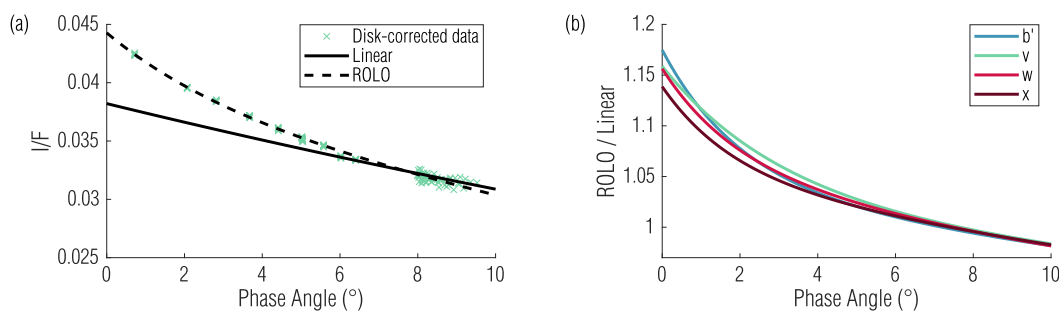


Fig. 11. Benu's moderate opposition surge is illustrated by comparing the Linear-Akimov and ROLO phase functions (a). Linear-Akimov is linear in magnitude space; ROLO has an opposition surge term. The ratio of the two models (b) shows an opposition magnitude of ~15%.

These data, taken while Benu subtended only a few dozen pixels, indicate a small opposition surge. We show these data for the *v* filter in Fig. 11(a) and overlay the Linear-Akimov and ROLO phase functions. The Linear-Akimov phase function is linear in magnitude space, whereas the ROLO phase function is polynomial and includes an exponential parameter to model the opposition surge (Table 2). Here we model the Linear-Akimov phase function using only data with phase angles $>7^\circ$. This ensures that low phase data do not perturb the linear model, while also including all of the Equatorial Stations data. The ROLO model uses all available data. Dividing the ROLO phase curve by the Linear-Akimov phase curve (Fig. 11(b)) illustrates that the opposition curve has a magnitude of $\sim 14\text{--}18\%$ and a half-width at half maximum of $\sim 2^\circ$. As expected, the peak is lower and broader than that of higher-albedo surfaces such as Eros (Domingue et al., 2002), Itokawa (Kitazato et al., 2008), and the Moon (Buratti et al., 1996). It is also somewhat lower and broader than the opposition effect seen on Ceres (Schröder et al., 2018), which is twice as bright as Benu. Although the surge magnitude increases slightly with decreasing wavelength, the change is on the same order as the uncertainties described in Section 4.5, thus we cannot confirm it with this analysis. The minimal spectral effect aligns with the common understanding that a single-scattering surface should not show a significant wavelength-dependent opposition surge (Buratti et al., 1996).

Benu's rough, heavily shadowed terrain, would suggest a surface dominated by shadow hiding. The relatively broad shape of Benu's opposition surge is in accordance with a prominent SHOE (Helfenstein et al., 1997). The dark, presumably single-scattering, surface should reduce the magnitude of the multiple-scattering component of the CBOE. However, the single-scattering component is likely still present, given Benu's roughness (Hapke, 2012). A slight inflection in the ROLO phase model at $\sim 2^\circ$ phase may hint at a CBOE, which is typically associated with a narrow opposition surge. Though we are limited by the sparsity of data at low phase, we expect that Hapke modeling of the surface will explore the opposition surge further and quantify the relative weight of the CBOE and SHOE components.

7. Conclusions

We present global photometric models for asteroid (101955) Benu. We calculate the models from images acquired by OCAMS during dedicated photometric imaging observation campaigns. The series of photometric models presented in this work show similar qualities of fit, with some subtle variations, are in agreement with ground-based measurements of Benu, and confirm a global albedo of 0.044 at 550 nm. The ROLO model is the only model to accommodate Benu's opposition surge and produces the best fit to the data. As such, we suggest the ROLO model for photometric correction of OCAMS images. However, the choice of disk function is strongly dependent on shape model resolution and may evolve in the future.

We observe a minor opposition surge and gentle phase reddening in the photometric models. These effects potentially result from the macroscopic roughness of the surface, which enables the shadow-hiding opposition effect and longer optical path lengths that increase the degree of phase reddening. The dramatic shadowing that results from Benu's rugged terrain creates challenges in both the photometric modeling and photometric correction processes, due to inaccurate measurements of incidence and emission angles on the surface. Subsequent work with higher-resolution, laser altimeter-based, shape models will account for the variation on Benu's surface. These efforts will produce a more accurate representation of Benu's photometric response, develop knowledge of the impact of shadows on small rubble-pile asteroids, and significantly improve the photometric correction of individual rocks and other features on Benu's surface.

Acknowledgments

The work presented here is a small part of a large mission, the success of which is due to the contributions of many individuals at many institutions. We thank all those who are part of the OSIRIS-REX team. This research has made use of the USGS Integrated Software for Imagers and Spectrometers (ISIS3). The image data, kernels, photometric models, and altimetry data in this work are archived in the Planetary Data System Small Bodies Node (Rizk et al., 2019) at <https://sbn.psi.edu/pds/resource/orex/> in accordance with the OSIRIS-REX Data Management Plan (Crombie et al., 2018). This material is based upon work supported by NASA under Contract NNM10AA11C issued through the New Frontiers Program. OLA and funding for the Canadian authors were provided by the Canadian Space Agency.

References

- Acton, C., Bachman, N., Semenov, B., Wright, E., 2018. A look towards the future in the handling of space science mission geometry. *Planet. Space Sci.* 150, 9–12. <https://doi.org/10.1016/j.pss.2017.02.013>.
- Barnouin, O.S., Daly, M.G., Palmer, E.E., Gaskell, R.W., Weirich, J.R., Johnson, C.L., Al Asad, M.M., Roberts, J.H., Perry, M.E., Susorney, H.C.M., Daly, R.T., Bierhaus, E.B., Seabrook, J.A., Espiritu, R.C., Nair, A.H., Nguyen, L., Neumann, G.A., Ernst, C.M., Boynton, W.V., Nolan, M.C., Adam, C.D., Moreau, M.C., Rizk, B., Drouet D'Aubigny, C.Y., Jawin, E.R., Walsh, K.J., Michel, P., Schwartz, S.R., Ballouz, R.-L., Mazarico, E.M., Scheeres, D.J., McMahon, J.W., Bottke, W.F., Sugita, S., Hirata, N., Hirata, N., Watanabe, S.-i., Burke, K.N., DellaGiustina, D.N., Bennett, C.A., Lauretta, D.S., 2019. Shape of (101955) Benu indicative of a rubble pile with internal stiffness. *Nat. Geosci.* 12, 247–252. <https://doi.org/10.1038/s41561-019-0330-x>.
- Barnouin, O.S., Daly, M.G., Palmer, E.E., Johnson, C.L., Gaskell, R.W., Al Asad, M., Bierhaus, E.B., Craft, K.L., Ernst, C.M., Espiritu, R.C., Contreras, J., Neumann, G.A., Nguyen, L., Nolan, M.C., Mazarico, E., Perry, M.E., Philpott, L.C., Roberts, J.H., Steele, R.J., Seabrook, J., Susorney, H.C.M., Weirich, J.R., Lauretta, D.S., 2020. Digital terrain mapping by the OSIRIS-REX mission. *Planet. Space Sci.* 180, 104764. <https://doi.org/10.1016/j.pss.2019.104764>.
- Bennett, C.A., DellaGiustina, D.N., Becker, K.J., Becker, T.L., Edmondson, K.L., Golish, D.R., Bennett, R.J., Burke, K.N., Cue, C.N.U., Clark, B.E., Contreras, J., Deshapriya, J.D.P., D'Aubigny, C.D., Fitzgibbon, G., Jawin, E.R., Nolan, T.Q., Porter, N.A., Riehl, M.M., Roper, H.L., Rizk, B., Tang, Y., Zeszut, Z., Gaskell, R.W., Palmer, E.E., Weirich, J.R., Al Asad, M.M., Philpott, L., Daly, M.G., Barnouin, O.S., Enos, H.L., Lauretta, D.S., 2020. A high-resolution global basemap of (101955) Benu. *Icarus* 113690. <https://doi.org/10.1016/j.icarus.2020.113690>.
- Berry, K., Sutter, B., May, A., Williams, K., Barbee, B.W., Beckman, M., Williams, B., 2013. OSIRIS-REX Touch-And-Go (TAG) Mission Design and Analysis, 36th Annual AAS Guidance and Control Conference, pp. 13–095.
- Buratti, B.J., Hillier, J.K., Wang, M., 1996. The lunar opposition surge: observations by Clementine. *Icarus* 124, 490–499. <https://doi.org/10.1006/icar.1996.0225>.
- Buratti, B.J., Hicks, M.D., Nettles, J., Staid, M., Pieters, C.M., Sunshine, J., Boardman, J., Stone, T.C., 2011. A wavelength-dependent visible and infrared spectrophotometric function for the Moon based on ROLO data. *J. Geophys. Res.* 116, E00G03. <https://doi.org/10.1029/2010JE003724>.
- Clark, B.E., Binzel, R.P., Howell, E.S., Cloutis, E.A., Ockert-Bell, M., Christensen, P., Barucci, M.A., DeMeo, F., Lauretta, D.S., Connolly, H., Soderberg, A., Hergenrother, C., Lim, L., Emery, J., Mueller, M., 2011. Asteroid (101955) 1999 RQ36: spectroscopy from 0.4 to 2.4 μm and meteorite analogs. *Icarus* 216, 462–475. <https://doi.org/10.1016/j.icarus.2011.08.021>.
- Crombie, M., Selznick, S., Loveridge, M., Rizk, B., DellaGiustina, D.N., Golish, D.R., Bos, B.J., Christensen, P.R., Hamilton, V.E., Reuter, D., Simon, A.A., Barnouin, O.S., Daly, M.G., Espiritu, R.C., Clark, B., Nolan, M.C., Lauretta, D.S., 2018. Schedule of Origins, Spectral Interpretation, Resource Identification, Security-Regolith Explorer Data Product Releases to the Planetary Data System, Abstract P33C-3858 Presented at 2018 Fall Meeting, AGU, Washington, D.C., 10–14 Dec.
- Daly, M.G., Barnouin, O.S., Dickinson, C., Seabrook, J., Johnson, C.L., Cunningham, G., Haltigin, T., Gaudreau, D., Brunet, C., Aslam, I., Taylor, A., Bierhaus, E.B., Boynton, W., Nolan, M., Lauretta, D.S., 2017. The OSIRIS-REX Laser Altimeter (OLA) investigation and instrument. *Space Sci. Rev.* 212, 899–924. <https://doi.org/10.1007/s11214-017-0375-3>.
- DellaGiustina, D.N., Bennett, C.A., Becker, K., Golish, D.R., Le Corre, L., Cook, D.A., Edmondson, K.L., Chojnacki, M., Sutton, S.S., Milazzo, M.P., Carcich, B., Nolan, M.C., Habib, N., Burke, K.N., Becker, T., Smith, P.H., Walsh, K.J., Getzandanner, K., Wibben, D.R., Leonard, J.M., Westermann, M.M., Polit, A.T., Kidd, J.N., Hergenrother, C.W., Boynton, W.V., Backer, J., Sides, S., Mapel, J., Berry, K., Roper, H., Drouet d'Aubigny, C., Rizk, B., Crombie, M.K., Kinney-Spano, E.K., de León, J., Rizos, J.L., Licandro, J., Campins, H.C., Clark, B.E., Enos, H.L., Lauretta, D.S., 2018. Overcoming the challenges associated with image-based mapping of small bodies in preparation for the OSIRIS-REX mission to (101955) Benu. *Earth Sp. Sci.* 5, 929–949. <https://doi.org/10.1029/2018EA000382>.
- DellaGiustina, D.N., Emery, J.P., Golish, D.R., Rozitis, B., Bennett, C.A., Burke, K.N., Ballouz, R.-L., Becker, K.J., Christensen, P.R., Drouet d'Aubigny, C.Y., Hamilton, V.E., Reuter, D.C., Rizk, B., Simon, A.A., Asphaug, E., Bandfield, J.L., Barnouin, O.S.,

- Barucci, M.A., Bierhaus, E.B., Binzel, R.P., Bottke, W.F., Bowles, N.E., Campins, H., Clark, B.C., Clark, B.E., Connolly, H.C., Daly, M.G., Leon, J. de, Delbo, M., Deshpandya, J.D.P., Elder, C.M., Fornasier, S., Hergenrother, C.W., Howell, E.S., Jawn, E.R., Kaplan, H.H., Kareta, T.R., Le Corre, L., Li, J.-Y., Licandro, J., Lim, L.F., Michel, P., Molaro, J., Nolan, M.C., Pajola, M., Popescu, M., Garcia, J.L.R., Ryan, A., Schwartz, S.R., Shultz, N., Siegler, M.A., Smith, P.H., Tatsumi, E., Thomas, C.A., Walsh, K.J., Wolner, C.W.V., Zou, X.-D., Lauretta, D.S., 2019. Properties of rubble-pile asteroid (101955) Bennu from OSIRIS-REx imaging and thermal analysis. *Nat. Astron.* 3, 341–351. <https://doi.org/10.1038/s41550-019-0731-1>.
- Denevi, B.W., Chabot, N.L., Murchie, S.L., Becker, K.J., Blewett, D.T., Domingue, D.L., Ernst, C.M., Hash, C.D., Hawkins, S.E., Keller, M.R., Laslo, N.R., Nair, H., Robinson, M.S., Seelos, F.P., Stephens, G.K., Turner, F.S., Solomon, S.C., 2018. Calibration, projection, and final image products of MESSENGER's Mercury dual imaging system. *Space Sci. Rev.* 214, 2. <https://doi.org/10.1007/s11214-017-0440-y>.
- Domingue, D.L., Robinson, M., Carcich, B., Joseph, J., Thomas, P., Clark, B.E., 2002. Disk-integrated photometry of 433 Eros. *Icarus* 155, 205–219. <https://doi.org/10.1006/icar.2001.6764>.
- Emery, J.P., Fernández, Y.R., Kelley, M.S.P., Warden (née Crane), K.T., Hergenrother, C., Lauretta, D.S., Drake, M.J., Campins, H., Ziffer, J., 2014. Thermal infrared observations and thermophysical characterization of OSIRIS-REx target asteroid (101955) Bennu. *Icarus* 234, 17–35. <https://doi.org/10.1016/j.icarus.2014.02.005>.
- Golish, D.R., Drouet d'Aubigny, C., Rizk, B., DellaGiustina, D.N., Smith, P.H., Becker, K., Shultz, N., Stone, T., Barker, M.K., Mazarico, E., Tatsumi, E., Gaskell, R.W., Harrison, L., Merrill, C., Fellows, C., Williams, B., O'Dougherty, S., Whiteley, M., Hancock, J., Clark, B.E., Hergenrother, C.W., Lauretta, D.S., 2020. Ground and in-flight calibration of the OSIRIS-REx camera suite. *Space Sci. Rev.* 216, 12. <https://doi.org/10.1007/s11214-019-0626-6>.
- Grady, J., Veverka, J., 1986. The wavelength dependence of phase coefficients. *Icarus* 66, 455–467. [https://doi.org/10.1016/0019-1035\(86\)90085-0](https://doi.org/10.1016/0019-1035(86)90085-0).
- Grott, M., Knollenberg, J., Hamm, M., Ogawa, K., Jaumann, R., Otto, K.A., Delbo, M., Michel, P., Biele, J., Neumann, W., Knapmeyer, M., Kührt, E., Senshu, H., Okada, T., Helbert, J., Maturilli, A., Müller, N., Hagermann, A., Sakatani, N., Tanaka, S., Arai, T., Mottola, S., Tachibana, S., Pelivan, L., Drube, L., Vincent, J.-B., Yano, H., Piloget, C., Matz, K.D., Schmitz, N., Koncz, A., Schröder, S.E., Trauthan, F., Schlotterer, M., Krause, C., Ho, T.-M., Moussi-Soffys, A., 2019. Low thermal conductivity boulder with high porosity identified on C-type asteroid (162173) Ryugu. *Nat. Astron.* <https://doi.org/10.1038/s41550-019-0832-x>.
- Gundlach, B., Blum, J., 2013. A new method to determine the grain size of planetary regolith. *Icarus* 223, 479–492. <https://doi.org/10.1016/j.icarus.2012.11.039>.
- Hamilton, V.E., Simon, A.A., Christensen, P.R., Reuter, D.C., Clark, B.E., Barucci, M.A., Bowles, N.E., Boynton, W.V., Brucato, J.R., Cloutis, E.A., Connolly, H.C., Donaldson Hanna, K.L., Emery, J.P., Enos, H.L., Fornasier, S., Haberle, C.W., Hanna, R.D., Howell, E.S., Kaplan, H.H., Keller, L.P., Lantz, C., Li, J.-Y., Lim, L.F., McCoy, T.J., Merlin, F., Nolan, M.C., Praet, A., Rozitis, B., Sandford, S.A., Schrader, D.L., Thomas, C.A., Zou, X.-D., Lauretta, D.S., 2019. Evidence for widespread hydrated minerals on asteroid (101955) Bennu. *Nat. Astron.* <https://doi.org/10.1038/s41550-019-0722-2>.
- Hapke, B., 1981. Bidirectional reflectance spectroscopy: 1. Theory. *J. Geophys. Res. Solid Earth* 86, 3039–3054. <https://doi.org/10.1029/JB086iB04p03039>.
- Hapke, B., 1986. Bidirectional reflectance spectroscopy 4. The extinction coefficient and the opposition effect. *Icarus* 67, 264–280. [https://doi.org/10.1016/0019-1035\(86\)90108-9](https://doi.org/10.1016/0019-1035(86)90108-9).
- Hapke, B., 2012. Theory of Reflectance and Emittance Spectroscopy, 2nd ed. Cambridge University Press, Cambridge. <https://doi.org/10.1017/CBO9781139025683>.
- Hapke, B.W., Nelson, R.M., Smythe, W.D., 1993. The opposition effect of the Moon: the contribution of coherent backscatter. *Science (80-)* 260, 509–511. <https://doi.org/10.1126/science.260.5107.509>.
- Helfenstein, P., Veverka, J., Hillier, J., 1997. The lunar opposition effect: a test of alternative models. *Icarus* 128, 2–14. <https://doi.org/10.1006/icar.1997.5726>.
- Hergenrother, C.W., Nolan, M.C., Binzel, R.P., Cloutis, E.A., Barucci, M.A., Michel, P., Scheeres, D.J., D'Aubigny, C.D., Lazzaro, D., Pinilla-Alonso, N., Campins, H., Licandro, J., Clark, B.E., Rizk, B., Beshore, E.C., Lauretta, D.S., 2013. Lightcurve, color and phase function photometry of the OSIRIS-REx target asteroid (101955) Bennu. *Icarus* 226, 663–670. <https://doi.org/10.1016/j.icarus.2013.05.044>.
- Hergenrother, C.W., Maleszewski, C.K., Nolan, M.C., Li, J.-Y., Drouet d'Aubigny, C.Y., Shelly, F.C., Howell, E.S., Kareta, T.R., Izawa, M.R.M., Barucci, M.A., Bierhaus, E.B., Campins, H., Chesley, S.R., Clark, B.E., Christensen, E.J., DellaGiustina, D.N., Fornasier, S., Golish, D.R., Hartzell, C.M., Rizk, B., Scheeres, D.J., Smith, P.H., Zou, X.-D., Lauretta, D.S., 2019. The operational environment and rotational acceleration of asteroid (101955) Bennu from OSIRIS-REx observations. *Nat. Commun.* 10, 1291. <https://doi.org/10.1038/s41467-019-09213-x>.
- Hicks, M.D., Buratti, B.J., Nettles, J., Staid, M., Sunshine, J., Pieters, C.M., Besse, S., Boardman, J., 2011. A photometric function for analysis of lunar images in the visual and infrared based on Moon mineralogy mapper observations. *J. Geophys. Res. E Planets* 116, 1–10. <https://doi.org/10.1029/2010JE003733>.
- Hillier, J.K., Buratti, B.J., Hill, K., 1999. Multispectral photometry of the Moon and absolute calibration of the Clementine UV/Vis camera. *Icarus* 141, 205–225. <https://doi.org/10.1006/icar.1999.6184>.
- Irvine, W.M., 1966. The shadowing effect in diffuse reflection. *J. Geophys. Res.* 71, 2931–2937. <https://doi.org/10.1029/JZ071i012p02931>.
- Jaumann, R., Schmitz, N., Ho, T.-M., Schröder, S.E., Otto, K.A., Stephan, K., Elgner, S., Krohn, K., Preusker, F., Scholten, F., Biele, J., Ulamec, S., Krause, C., Sugita, S., Matz, K.-D., Roatsch, T., Parekh, R., Mottola, S., Grott, M., Michel, P., Trauthan, F., Koncz, A., Michaelis, H., Lange, C., Grundmann, J.T., Maibaum, M., Sasaki, K., Wolff, F., Reill, J., Moussi-Soffys, A., Lorda, L., Neumann, W., Vincent, J.-B., Wagner, R., Bibring, J.-P., Kameda, S., Yano, H., Watanabe, S., Yoshikawa, M., Tsuda, Y., Okada, T., Yoshimitsu, T., Mimasu, Y., Saiki, T., Yabuta, H., Rauer, H., Honda, R., Morota, T., Yokota, Y., Kouyama, T., 2019. Images from the surface of asteroid Ryugu show rocks similar to carbonaceous chondrite meteorites. *Science* 365, 817–820. <https://doi.org/10.1126/science.aaw8627>.
- Kaasalainen, M., 2001. Optimization methods for asteroid lightcurve inversion II. The complete inverse problem. *Icarus* 153, 37–51. <https://doi.org/10.1006/icar.2001.6674>.
- Keszthelyi, L., Becker, T., Sides, S., Barrett, J., Cook, D., Lambricht, S., Lee, E., Milazzo, M., Oyama, K., Richie, J., Saleh, R., Shinaman, J., Sucharski, T., Titus, T., Waddren, J., Weller, L., 2013. Support and future vision for the Integrated Software for Imagers and Spectrometers (ISIS). In: *44th Lunar Planet. Sci. Conf.* 44, p. 2546.
- Kieffer, H.H., Wildey, R.L., 1996. Establishing the Moon as a spectral radiance standard. *J. Atmos. Ocean. Technol.* 13, 360–375. [https://doi.org/10.1175/1520-0426\(1996\)013<0360:ETMAAS>2.0.CO;2](https://doi.org/10.1175/1520-0426(1996)013<0360:ETMAAS>2.0.CO;2).
- Kitazato, K., Clark, B.E., Abe, M., Abe, S., Takagi, Y., Hiroi, T., Barnouin-Jha, O.S., Abell, P.A., Lederer, S.M., Vilas, F., 2008. Near-infrared spectrophotometry of Asteroid 25143 Itokawa from NIRS on the Hayabusa spacecraft. *Icarus* 194, 137–145. <https://doi.org/10.1016/j.icarus.2007.08.029>.
- Kreslavsky, M.A., Shkuratov, Y.G., Velikodsky, Y.I., Kaydash, V.G., Stankevich, D.G., Pieters, C.M., 2000. Photometric properties of the lunar surface derived from Clementine observations. *J. Geophys. Res. Planets* 105, 20281–20295. <https://doi.org/10.1029/1999JE001150>.
- Lauretta, D.S., Balram-Knutson, S.S., Beshore, E., Boynton, W.V., Drouet d'Aubigny, C., DellaGiustina, D.N., Enos, H.L., Golish, D.R., Hergenrother, C.W., Howell, E.S., Bennett, C.A., Morton, E.T., Nolan, M.C., Rizk, B., Roper, H.L., Bartels, A.E., Bos, B. J., Dworkin, J.P., Highsmith, D.E., Lorenz, D.A., Lim, L.F., Mink, R., Moreau, M.C., Nuth, J.A., Reuter, D.C., Simon, A.A., Bierhaus, E.B., Bryan, B.H., Ballouz, R., Barnouin, O.S., Binzel, R.P., Bottke, W.F., Hamilton, V.E., Walsh, K.J., Chesley, S.R., Christensen, P.R., Clark, B.E., Connolly, H.C., Crombie, M.K., Daly, M.G., Emery, J. P., McCoy, T.J., McMahon, J.W., Scheeres, D.J., Messenger, S., Nakamura-Messenger, K., Righter, K., Sandford, S.A., 2017. OSIRIS-REx: sample return from asteroid (101955) Bennu. *Space Sci. Rev.* 212, 925–984. <https://doi.org/10.1007/s11214-017-0405-1>.
- Lauretta, D.S., DellaGiustina, D.N., Bennett, C.A., Golish, D.R., Becker, K.J., Balram-Knutson, S.S., Barnouin, O.S., Becker, T.L., Bottke, W.F., Boynton, W.V., Campins, H., Clark, B.E., Connolly, H.C., Drouet d'Aubigny, C.Y., Dworkin, J.P., Emery, J.P., Enos, H.L., Hamilton, V.E., Hergenrother, C.W., Howell, E.S., Izawa, M. R.M., Kaplan, H.H., Nolan, M.C., Rizk, B., Roper, H.L., Scheeres, D.J., Smith, P.H., Walsh, K.J., Wolner, C.W.V., 2019. The unexpected surface of asteroid (101955) Bennu. *Nature* 568, 55–60. <https://doi.org/10.1038/s41586-019-1033-6>.
- Li, J., A'Hearn, M.F., McFadden, L.A., 2004. Photometric analysis of Eros from NEAR data. *Icarus* 172, 415–431. <https://doi.org/10.1016/j.icarus.2004.07.024>.
- Li, J.-Y., Le Corre, L., Schröder, S.E., Reddy, V., Denevi, B.W., Buratti, B.J., Mottola, S., Hoffmann, M., Gutierrez-Marques, P., Nathues, A., Russell, C.T., Raymond, C.A., 2013. Global photometric properties of Asteroid (4) Vesta observed with Dawn Framing Camera. *Icarus* 226, 1252–1274. <https://doi.org/10.1016/j.icarus.2013.08.011>.
- Li, J.-Y., Helfenstein, P., Buratti, B., Takir, D., Clark, B.E., 2015. Asteroid Photometry, Asteroids IV. University of Arizona Press, Tucson, AZ, pp. 277–326. https://doi.org/10.2458/azu_uapress_9780816532131-ch007.
- Li, J.-Y., Reddy, V., Nathues, A., Corre, L. Le, Izawa, M.R.M., Cloutis, E.A., Sykes, M.V., Carsenty, U., Castillo-Rogez, J.C., Hoffmann, M., Jaumann, R., Krohn, K., Mottola, S., Prettyman, T.H., Schaefer, M., Schenk, P., Schröder, S.E., Williams, D.A., Smith, D.E., Zuber, M.T., Konopliv, A.S., Park, R.S., Raymond, C.A., Russell, C.T., 2016. Surface albedo and spectral variability of Ceres. *Astrophys. J.* 817, L22. <https://doi.org/10.3847/2041-8205/817/2/L22>.
- Li, J., Schröder, S.E., Mottola, S., Nathues, A., Castillo-Rogez, J.C., Schorghofer, N., Williams, D.A., Ciarniello, M., Longobardo, A., Raymond, C.A., Russell, C.T., 2019. Spectrophotometric modeling and mapping of Ceres. *Icarus* 322, 144–167. <https://doi.org/10.1016/j.icarus.2018.12.038>.
- Longobardo, A., Palomba, E., Ciarniello, M., Tosi, F., De Sanctis, M.C., Capaccioni, F., Zambon, F., Ammannito, E., Filacchione, G., Raymond, C.A., 2016. Disk-resolved photometry of Vesta and Lutetia and comparison with other asteroids. *Icarus* 267, 204–216. <https://doi.org/10.1016/j.icarus.2015.12.025>.
- Longobardo, A., Palomba, E., Galiano, A., De Sanctis, M.C., Ciarniello, M., Raponi, A., Tosi, F., Schröder, S.E., Carrozzo, F.G., Ammannito, E., Zambon, F., Stephan, K., Capria, M.T., Rognini, E., Raymond, C.A., Russell, C.T., 2019. Photometry of Ceres and Occator faculae as inferred from VIR/Dawn data. *Icarus* 320, 97–109. <https://doi.org/10.1016/j.icarus.2018.02.022>.
- Markwardt, C.B., 2008. Non-linear least squares fitting in IDL with MPFIT. In: *Lewis, J., Argyle, R., Bunclark, P., Evans, D., Gonzales-Solares, E. (Eds.), Astronomical Data Analysis Software and Systems, ASP Conference Series*, p. A.16.
- Masoumzadeh, N., Boehnhardt, H., Li, J.Y., Vincent, J.B., 2015. Photometric analysis of Asteroid (21) Lutetia from Rosetta-OSIRIS images. *Icarus* 257, 239–250. <https://doi.org/10.1016/j.icarus.2015.05.013>.
- McEwen, A.S., 1986. Exogenic and endogenic albedo and color patterns on Europa. *J. Geophys. Res.* 91, 8077. <https://doi.org/10.1029/JB091iB08p08077>.
- McEwen, A.S., 1991. Photometric functions for photoclinometry and other applications. *Icarus* 92, 298–311. [https://doi.org/10.1016/0019-1035\(91\)90053-V](https://doi.org/10.1016/0019-1035(91)90053-V).
- Minnaert, M., 1941. The reciprocity principle in lunar photometry. *Astrophys. J.* 93, 403. <https://doi.org/10.1086/144279>.
- Muñón, K., Piironen, J., Shkuratov, Y.G., Ovcharenko, A., Clark, B.E., 2002. Asteroid photometric and polarimetric phase effects. In: *Bottke, W.F., Cellino, A., Paolich, P., Binzel, R. (Eds.), Asteroids III*, pp. 123–138.

- Pilorget, C., Fernando, J., Ehlmann, B.L., Schmidt, F., Hiroi, T., 2016. Wavelength dependence of scattering properties in the VIS-NIR and links with grain-scale physical and compositional properties. *Icarus* 267, 296–314. <https://doi.org/10.1016/j.icarus.2015.12.029>.
- Rizk, B., Drouet d'Aubigny, C., Golish, D., Fellows, C., Merrill, C., Smith, P., Walker, M. S., Hendershot, J.E., Hancock, J., Bailey, S.H., DellaGiustina, D.N., Lauretta, D.S., Tanner, R., Williams, M., Harshman, K., Fitzgibbon, M., Verts, W., Chen, J., Connors, T., Hamara, D., Dowd, A., Lowman, A., Dubin, M., Burt, R., Whiteley, M., Watson, M., McMahon, T., Ward, M., Booher, D., Read, M., Williams, B., Hunten, M., Little, E., Saltzman, T., Alfred, D., O'Dougherty, S., Walthall, M., Kenagy, K., Peterson, S., Crowther, B., Perry, M.L., See, C., Selznick, S., Sauve, C., Beiser, M., Black, W., Pfisterer, R.N., Lancaster, A., Oliver, S., Oquest, C., Crowley, D., Morgan, C., Castle, C., Dominguez, R., Sullivan, M., 2018. OCAMS: the OSIRIS-REx camera suite. *Space Sci. Rev.* 214, 26. <https://doi.org/10.1007/s11214-017-0460-7>.
- Rizk, B., Drouet d'Aubigny, C., Golish, D.R., DellaGiustina, D.N., Lauretta, D.S., 2019. Origins, Spectral Interpretation, Resource Identification, Security, Regolith Explorer (OSIRIS-REx). OSIRIS-REx Camera Suite (OCAMS) Bundle [urn:nasa:pds:orex.ocams](https://nasa.pds.orex.ocams).
- Schröder, S.E., Mottola, S., Keller, H.U., Raymond, C.A., Russell, C.T., 2013. Resolved photometry of Vesta reveals physical properties of crater regolith. *Planet. Space Sci.* 85, 198–213. <https://doi.org/10.1016/j.pss.2013.06.009>.
- Schröder, S.E., Grynko, Y., Pommerol, A., Keller, H.U., Thomas, N., Roush, T.L., 2014. Laboratory observations and simulations of phase reddening. *Icarus* 239, 201–216. <https://doi.org/10.1016/j.icarus.2014.06.010>.
- Schröder, S.E., Mottola, S., Carsenty, U., Ciarniello, M., Jaumann, R., Li, J.-Y., Longobardo, A., Palmer, E., Pieters, C., Preusker, F., Raymond, C.A., Russell, C.T., 2017. Resolved spectrophotometric properties of the Ceres surface from Dawn Framing Camera images. *Icarus* 288, 201–225. <https://doi.org/10.1016/j.icarus.2017.01.026>.
- Schröder, S.E., Li, J.-Y., Rayman, M.D., Joy, S.P., Polanskey, C.A., Carsenty, U., Castillo-Rogez, J.C., Ciarniello, M., Jaumann, R., Longobardo, A., McFadden, L.A., Mottola, S., Sykes, M., Raymond, C.A., Russell, C.T., 2018. Ceres' opposition effect observed by the Dawn framing camera. *Astron. Astrophys.* 620, A201. <https://doi.org/10.1051/0004-6361/201833596>.
- Shkuratov, Y., Kaydash, V., Korokhin, V., Velikodsky, Y., Opanasenko, N., Videen, G., 2011. Optical measurements of the Moon as a tool to study its surface. *Planet. Space Sci.* 59, 1326–1371. <https://doi.org/10.1016/j.pss.2011.06.011>.
- Spjuth, S., Jorda, L., Lamy, P.L., Keller, H.U., Li, J.Y., 2012. Disk-resolved photometry of Asteroid (2867) Steins. *Icarus* 221, 1101–1118. <https://doi.org/10.1016/j.icarus.2012.06.021>.
- Sugita, S., Honda, R., Morota, T., Kameda, S., Sawada, H., Tatsumi, E., Yamada, M., Honda, C., Yokota, Y., Kouyama, T., Sakatani, N., Ogawa, K., Suzuki, H., Okada, T., Namiki, N., Tanaka, S., Iijima, Y., Yoshioka, K., Hayakawa, M., Cho, Y., Matsuoka, M., Hirata, N., Hirata, N., Miyamoto, H., Domingue, D., Hirabayashi, M., Nakamura, T., Hiroi, T., Michikami, T., Michel, P., Ballouz, R.-L., Barnouin, O.S., Ernst, C.M., Schröder, S.E., Kikuchi, H., Hemmi, R., Komatsu, G., Fukuhara, T., Taguchi, M., Arai, T., Senshu, H., Demura, H., Ogawa, Y., Shimaki, Y., Sekiguchi, T., Müller, T.G., Hagermann, A., Mizuno, T., Noda, H., Matsumoto, K., Yamada, R., Ishihara, Y., Ikeda, H., Araki, H., Yamamoto, K., Abe, S., Yoshida, F., Higuchi, A., Sasaki, S., Oshigami, S., Tsuruta, S., Asari, K., Tazawa, S., Shizugami, M., Kimura, J., Otsubo, T., Yabuta, H., Hasegawa, S., Ishiguro, M., Tachibana, S., Palmer, E., Gaskell, R., Le Corre, L., Jaumann, R., Otto, K., Schmitz, N., Abell, P.A., Barucci, M. A., Zolensky, M.E., Vilas, F., Thuillet, F., Sugimoto, C., Takaki, N., Suzuki, Y., Kamiyoshihara, H., Okada, M., Nagata, K., Fujimoto, M., Yoshikawa, M., Yamamoto, Y., Shirai, K., Noguchi, R., Ogawa, N., Terui, F., Kikuchi, S., Yamaguchi, T., Oki, Y., Takao, Y., Takeuchi, H., Ono, G., Mimasu, Y., Yoshikawa, K., Takahashi, T., Takei, Y., Fujii, A., Hirose, C., Nakazawa, S., Hosoda, S., Mori, O., Shimada, T., Soldini, S., Iwata, T., Abe, M., Yano, H., Tsukizaki, R., Ozaki, M., Nishiyama, K., Saiki, T., Watanabe, S., Tsuda, Y., 2019. The geomorphology, color, and thermal properties of Ryugu: implications for parent-body processes. *Science*. <https://doi.org/10.1126/science.aaw0422>.
- Takir, D., Clark, B.E., Drouet d'Aubigny, C., Hergenrother, C.W., Li, J., Lauretta, D.S., Binzel, R.P., 2015. Photometric models of disk-integrated observations of the OSIRIS-REx target Asteroid (101955) Bennu. *Icarus* 252, 393–399. <https://doi.org/10.1016/j.icarus.2015.02.006>.
- Yokota, Y., Matsunaga, T., Ohtake, M., Haruyama, J., Nakamura, R., Yamamoto, S., Ogawa, Y., Morota, T., Honda, C., Saiki, K., Nagasawa, K., Kitazato, K., Sasaki, S., Iwasaki, A., Demura, H., Hirata, N., Hiroi, T., Honda, R., Iijima, Y., Mizutani, H., 2011. Lunar photometric properties at wavelengths 0.5–1.6 μm acquired by SELENE spectral profiler and their dependency on local albedo and latitudinal zones. *Icarus* 215, 639–660. <https://doi.org/10.1016/j.icarus.2011.07.028>.
- Zellner, B., Tholen, D.J., Tedesco, E.F., 1985. The eight-color asteroid survey: results for 589 minor planets. *Icarus* 61, 355–416. [https://doi.org/10.1016/0019-1035\(85\)90133-2](https://doi.org/10.1016/0019-1035(85)90133-2).
- Zou, X.-D., Li, J.-Y., Clark, B.E., Golish, D.R., Reuter, D.C., Simon, A.A., Hamilton, V.E., Lauretta, D.S., OSIRIS-Rex Team, 2019. Preliminary Analysis of the Photometric Properties of Asteroid (101955) Bennu From OVIRS Observations, 50th Lunar and Planetary Science Conference.